Near-wall lubricating layer in drag-reduced flows of rigid polymers

Lucas Warwaruk and Sina Ghaemi*
Department of Mechanical Engineering, University of Alberta, Edmonton, Alberta, Canada T6G 1H9

(Received 1 October 2021; accepted 26 May 2022; published 29 June 2022)

The current theories on the mechanism for polymer drag reduction (DR) are generally applicable for long-chain flexible polymers that form viscoelastic solutions. Rigid polymer solutions that generate DR seemingly lack prevalent viscoelastic characteristics. They do however demonstrate higher viscosities and a noticeable shear-thinning trend, approximated by generalized Newtonian models. The following experimental investigation scrutinizes the flow statistics of an aqueous xanthan gum solution in a turbulent channel flow, with friction Reynolds numbers Re_τ between 170 and 700. The amount of DR varies insignificantly between 27% and 33%. The velocity field is measured using planar particle image velocimetry and the steady shear rheology is measured using a torsional rheometer. The results are used to characterize the flow statistics of the polymer drag-reduced flows at different Re_τ and with negligible changes in DR, a parametric study only previously considered by numerical simulations. Changes to the mean velocity and Reynolds stress profiles with increasing Re_τ are similar to the modifications observed in Newtonian turbulence. Specifically, the inner-normalized mean velocity profiles overlap for different Re_τ and the Reynolds stresses monotonically grow in magnitude with increasing Re_τ. Profiles of mean viscosity with respect to the wall-normal position demonstrate a thin layer that consists of a low-viscosity fluid in the immediate vicinity of the wall. Fluid outside this thin layer has a significantly higher viscosity. We surmise that the demarcation in the mean shear viscosity between the inner lubricating layer and the outer layer cultivates fluid slippage in the buffer layer and an upward shift in the logarithmic layer, a hypothesis akin to DR using wall lubrication and superhydrophobic surfaces.

DOI: 10.1103/PhysRevFluids.7.064605

I. INTRODUCTION

Adding small quantities of high-molecular-weight polymers to a turbulent wall flow can produce a large reduction in skin friction relative to the solvent alone. This phenomenon was first discovered by Toms [1] and has since been actively studied. The most readily used drag-reducing polymers are long-chain flexible molecules that form viscoelastic non-Newtonian solutions. When these flexible polymer solutions are subjected to large amounts of shear (for example, through a pump, fitting, or a restriction) the solution undergoes mechanical degradation and becomes less effective at mitigating drag [2]. Therefore, flexible polymers are often used as a method for cost saving or performance enhancement in once-through fluid transport systems such as crude oil pipelines, fire suppression, or municipal sewage [3–5]. Mechanical degradation can be reduced by utilizing a polymer with a rigid molecular structure; however, this may require higher additive concentrations and a sacrifice in the amount of drag reduction (DR) [6]. While flexible polymers may coil and stretch within the turbulent flow, rigid polymers are believed to remain elongated at all times, regardless of the imposing flow field [7]. Rigid drag-reducing polymers are often naturally occurring polysaccharides

*ghaemi@ualberta.ca

that come in many different variants [6–10]. While DR using flexible polymers has been readily studied, investigations of rigid polymer DR are much less abundant. Existing comparisons seem to imply that flexible and rigid polymers mitigate drag in entirely unique manners [11–13]. However, additional investigations are needed to support such a conclusion. The following overview details the previous theoretical and experimental findings pertinent to polymer DR using flexible and rigid molecules.

Two existing theories attempt to elucidate how polymers interact with turbulence and reduce drag. In Lumley's viscous theory of DR, polymers are believed to damp turbulent structures due to an enhanced extensional viscosity in regions of the flow that experience significant elongational deformation rates [14]. The cogency of Lumley's viscous theory is conditional on polymer solutions having a large Trouton ratio $\mathrm{Tr} = \mu_{\mathrm{ext}}/\mu > 3$ and Weissenberg number $\mathrm{Wi} = \lambda_{\mathrm{ext}}/\tau_f > \frac{1}{2}$. Here μ_{ext} is the extensional viscosity, μ is the shear viscosity, λ_{ext} is the extensional relaxation time, and τ_f is a representative timescale of the turbulent flow. The elastic theory, proposed by de Gennes [15], suggested that a large μ_{ext} is not critical for DR. Instead DR occurs when the elastic stresses of the polymers become comparable to the Reynolds stresses of the flow. Regardless of the validity of one theory over the other, both rely on the polymer solution having some amount of viscoelasticity. This is despite the insinuation that the name of Lumley's viscous theory may prescribe, a caveat that has been alluded to by other authors as well [16,17]. Indeed, the results of pipe and channel flow experiments using flexible polymers have demonstrated a positive correlation between the amount of DR and the Wi of the flow [18]. Also, investigations using direct numerical simulation (DNS) with viscoelastic constitutive equations, such as the molecular finitely extensible nonlinear elastic dumbbell model with a Peterlin approximation (FENE-P) and the continuum-based Oldroyd-B model, have demonstrated good agreement in trends of skin friction, mean velocity, and Reynolds stresses, when compared with experimental results using flexible polymers [19–21]. All analytical, experimental, and numerical evidence leads us to believe that viscoelasticity is a necessity for polymer DR. However, rheological measurements of dilute rigid polymer solutions exhibit little extensional and elastic characteristics, despite being able to produce DR similar to flexible polymer solutions [6,13,22]. Comparisons of each solution's rheology can directly quantify the unique material characteristics of the two solutions.

Numerous experimental investigations have measured the shear and extensional rheology of flexible and rigid polymer solutions [13,18,23]. Mohammadtabar *et al.* [23] directly compared μ_{ext} of solutions of different drag-reducing flexible and rigid polymer species using a capillary breakup extensional rheometer (CABER). Their results reflected that drag-reducing flexible polymer solutions, with concentrations as low as 20 ppm, can exhibit Tr as large as 100 [23]. The implication is that flexible polymer solutions are viscoelastic ($\mathrm{Tr} > 3$) and effective at resisting elongational strain rates [24]. For the rigid polymer solutions, Mohammadtabar *et al.* [23] found that the extensional properties of the solution were immeasurable using the CABER apparatus, an observation not uncommon among experimentalists [8,13,22,23]. Attempts at measuring μ_{ext} for rigid polymer solutions using a CABER often fail, potentially due to low μ_{ext} and Tr [13,22,23]. However, the lack of extensional resistance in dilute rigid polymer solutions appears to be replaced by a higher shear viscosity and a more pronounced shear-thinning quality when contrasted with solutions of flexible polymers that produce similar quantities of DR [13,22,23]. Shear viscosity measurements of rigid polymer solutions are well approximated by shear-thinning generalized Newtonian (GN) models such as the Carreau-Yasuda or Cross models [24–26]. Based on existing measurements, a well-defined shear-thinning trend is the only obvious rheological trait for low-concentration solutions of drag-reducing rigid polymers [13,23]. The rheological measurements of flexible and rigid polymer solutions suggest that the two additives have different mechanisms for promoting DR.

Further evidence for a unique DR mechanism among flexible and rigid polymers is demonstrated by differences in some of their flow statistics. The most apparent distinction is their unique trajectories for attaining the maximum drag-reduction (MDR) asymptote in the skin-friction coefficient C_f with increasing polymer concentration or Reynolds number Re. Virk and Wagger [11] defined

flexible additives as type A drag reducers and rigid additives as being type B, based on their different trends in C_f versus Re. Despite their unique trends in C_f, flexible and rigid polymers share similarities in their mean velocity profiles. Escudier *et al.* [22] and Mohammadtabar *et al.* [12] demonstrated that mean velocity profiles of drag-reduced channel flows using rigid polymers were consistent with the elastic sublayer model, derived using mostly flexible polymers by Virk [27]. On the other hand, some authors have suggested that the two solutions modify the Reynolds stresses differently. In a recent review publication, Xi [17] stated that rigid polymers and flexible polymers produce different changes to the streamwise Reynolds stress profile during the transition from low drag reduction (LDR) to high drag reduction (HDR). Xi [17] made this observation based on the measurements by Escudier *et al.* [22] and Mohammadtabar *et al.* [12]. However, Xi [17] also noted that a good portion of the modifications to the Reynolds stresses could be attributed to differences in Re, something demonstrated explicitly by Thais *et al.* [28] using DNS and FENE-P, but seldom explored experimentally. Warwaruk and Ghaemi [13] compared the Reynolds stresses of flexible and rigid polymers for flows at HDR and MDR. They observed inconsistencies in the Reynolds stresses for drag-reduced flows of similar DR and concluded that the differences are primarily attributed to discrepancies in Re. Generally, it is not sufficiently well understood how the first- and second-order flow statistics of rigid polymer flows depend on Re and DR [16,22]. Few if any investigations have explicitly measured changes in the mean velocity profile and Reynolds stresses of drag-reducing rigid polymer solutions with varying Re that are independent of variations in DR.

Although the two most cited theories for polymer DR rely on viscoelasticity being a constituent property of the polymer solution, there is one phenomenological model that simulates polymer DR using a viscous approximation. L'vov *et al.* [29], De Angelis *et al.* [30], and Procaccia *et al.* [31] demonstrated that polymer DR can be approximated by a simulation of the Navier-Stokes equations using an effective viscosity that is a function of the wall-normal distance from the wall, i.e., y. Their effective viscosity profile was a piecewise function, where in the linear viscous sublayer the effective viscosity was constant, but in the buffer and logarithmic layers the effective viscosity grew linearly with increasing y. L'vov *et al.* [29] and De Angelis *et al.* [30] derived and simulated the model based on simplifications done to the viscoelastic FENE-P constitutive equations, a model noted as being representative of flexible polymers. Procaccia *et al.* [31] expressed that such an effective viscosity model could also be viable for modeling the drag-reduced flow of rigid polymer solutions as well. Instead of using FENE-P, Procaccia *et al.* [31] derived the effective viscosity model for rigid polymers based on a constitutive equation derived by Doi and Edwards [32] for dilute solutions of rodlike molecules. However, given the innate shear-thinning quality of rigid polymer solutions coupled with the mean wall-normal velocity gradient in a turbulent wall flow, an effective viscosity that increases with respect to the wall-normal distance is inherent in the turbulent wall flow of rigid polymer solutions. Indeed, DNS using GN shear-thinning constitutive equations demonstrates a spatially varying mean viscosity profile, where the viscosity is relatively constant near the solid boundary, but increases logarithmically in the buffer and logarithmic layers along y [33–36]. Although the wall-normal trend in the mean viscosity for GN fluids is different than the linear effective viscosity profile used by De Angelis *et al.* [30], it is clear that wall-normal variations in the viscosity may play an important role in DR. Therefore, an experimental investigation that evaluates the wall-normal viscosity profile of a rigid polymer solution is warranted.

The present investigation has two central objectives. The first is to provide high-fidelity turbulence statistics of a drag-reduced channel flow of rigid polymers with varying Re. Few experiments of rigid polymers have explored the effect of Re on flow statistics. The existing measurements of rigid polymers in a turbulent channel flow have low spatial resolutions [22] or appear to be in an arguably transitional flow regime due to small Re [12]. To alleviate this gap in the research, an experimental investigation is performed for a 170 ppm xanthan gum (XG) solution in a turbulent channel flow with a friction Reynolds number Re_τ between 170 and 700. The resulting levels of DR are between 27% and 33%, demonstrating little dependence on Re. Planar particle image velocimetry (PIV) measurements are used to measure the instantaneous velocity of the drag-reduced flows. Shear rheology is characterized using a double gap and a parallel plate geometry to capture

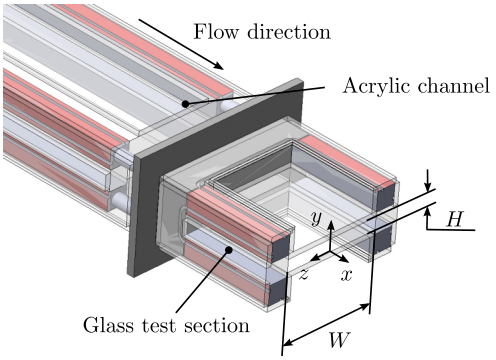

FIG. 1. Isometric cross section of the glass test section.

the viscosity of the XG solution over a large range of shear rates. The second objective of our paper is to elucidate a mechanism for rigid polymer DR from the perspective of lubricated flows. We observe a thin layer of low-viscosity fluid near the wall for the rigid polymer solution at all flow conditions, which is proposed to be essential for DR using rigid polymers.

II. EXPERIMENTAL METHODOLOGY

A. Flow facility

Experiments were performed in a recirculating flow facility with a channel section dedicated for flow measurements. A portion of the loop had a rectangular cross section of height H of 15 mm and width W of 120 mm, as shown in Fig. 1. Walls of the channel were cast acrylic, with the exception of one segment, the test section, where the walls were glass. Flow measurements using PIV were performed in the glass test section, which was situated approximately $107H$ downstream of the inlet to the channel portion. In total, the channel portion of the loop was $168H$ in length. Gradual transition fittings were used to connect the channel section to the remainder of the loop, which was a 2-in. nominal pipe. Additional details pertaining to the flow facility can be found in Ref. [13]. Figure 1 displays the Cartesian coordinate system with reference to the cross section of the glass test section. The standard right-hand orthonormal basis was used, with positions along the streamwise, wall-normal, and spanwise directions denoted by x, y, and z, respectively. The coordinate system was placed at the midspan of the lower channel wall within the laser sheet.

A centrifugal pump (LCC-M 50-230, GIW Industries Inc.) and a variable frequency drive (VFD) were used to propel the fluid within the loop. A shell and tube heat exchanger and a thermocouple were used to maintain a constant fluid temperature of $25\,^{\circ}\mathrm{C} \pm 0.3\,^{\circ}\mathrm{C}$. A Coriolis flow meter (Micro Motion F-series, Emerson Process Management) with an accuracy of $\pm 0.2\%$ was used to measure the mass flow rate $\dot{m}$ of the moving fluid. To maintain a constant $\dot{m}$, a proportional-integral-derivative controller, developed using LabView software (LabView 2015, National Instruments), was used to manipulate the frequency of the VFD and the rotational speed of the pump. The linear streamwise gradient in static pressure $\Delta P/\Delta x$ was measured using a differential pressure transducer (DP15, Validyne) equipped with a 1-psi diaphragm. Pressure ports were separated by $\Delta x = 109H$. The upstream port was situated $34H$ from the inlet of the channel.

Measurements were conducted for seven different conditions of bulk velocity $U_b = \dot{m}/\rho HW$, all of which are shown in Table I for water. Here ρ is the fluid density. In the case of water, the Reynolds number $\mathrm{Re} = \rho U_b H/\mu_w$ was between 9100 and 37 000. The symbol μ_w represents the dynamic viscosity of the fluid corresponding to the shear rate at the wall. While this is a variable for the polymer solutions, for a Newtonian fluid such as water, the dynamic viscosity is consistently 0.89 mPa s at $25\,^{\circ}\mathrm{C}$ [37,38]. Therefore, the Re of the polymer solutions are calculated later in

TABLE I. Flow properties for channel flow of water.

U_b (m s^{-1})	Re	ΔP (Pa)	τ_w (Pa)	u_τ (mm s^{-1})	λ (μm)	Re$_\tau$
0.542	9100	231	1.061	32.6	27.4	270
0.819	13800	477	2.188	46.8	19.1	390
1.094	18400	795	3.648	60.5	14.8	510
1.371	23000	1179	5.407	73.6	12.1	620
1.647	27700	1627	7.465	86.5	10.3	730
1.924	32300	2139	9.814	99.2	9.0	830
2.197	37000	2711	12.437	111.7	8.0	940

Sec. II D, when the wall shear rates and steady shear viscosity are obtained. The wall shear stress τ_w was established using measurements of the streamwise pressure gradient, i.e., $\tau_w = h\Delta P/\Delta x$, where $h = H/2$ is the half-channel height. The friction velocity $u_\tau = (\tau_w/\rho)^{1/2}$, wall units $\lambda = \mu_w/u_\tau\rho$, and friction Reynolds number $\mathrm{Re}_\tau = \rho u_\tau h/\mu_w$ were then subsequently determined, the results for which are listed in Table I for the flow of water.

B. Rigid polymer solution

The rigid polymer species considered in this investigation was the polysaccharide XG from Sigma Aldrich (CAS No. 1138-66-2). Solid XG, in powder form, was weighed using a digital scale (AB104-S, Mettler Toledo) with a 0.1 mg resolution. The powder was then gradually added to 15 l of tap water and agitated using a stand mixer (Model 1750, Arrow Engineering Mixing Products). The concentrated 15 l master solution was then left to rest overnight for approximately 12 h. The following day, the master solution was added to 100 l of moving tap water within the flow loop. This diluted the master solution to the desired concentration of 170 ppm. A 170 ppm solution of XG produced a solution of good transparency for PIV measurements. To ensure the solution was homogeneous, the pump was operated at 1400 rpm ($U_b = 4.380$ m s^{-1}) for 1 h. Near the end of the 1 h duration, ΔP was marginally growing at a rate of approximately 10 Pa min^{-1}, about a 0.1% increase in ΔP every minute. This was considered sufficiently steady state. After the 1 h time mark, the pump speed was reduced to 800 rpm, corresponding to $U_b = 2.197$ m s^{-1}, for the first PIV measurement at the highest Re. The pump speed was then reduced in increments such that PIV measurements for each flow condition listed in Table II were taken. At all of the measured flow rates listed in Table II, no variation in ΔP was observed during the PIV acquisition time. Therefore, any mechanical degradation or polymer deagglomeration was likely negligible after the 1-h mixing phase. Finally, fluid samples were collected for shear viscosity measurements using an access port along the flow loop.

TABLE II. Flow properties for channel flow of 170 ppm XG solution.

U_b (m s^{-1})	Re	$\mathcal{D}$ (%)	μ_w (mPa s)	u_τ (mm s^{-1})	λ (μm)	Re$_\tau$
0.542	6200	27	1.285	29.2	44.1	170
0.819	10500	30	1.152	40.6	28.5	260
1.094	14800	31	1.087	51.4	21.2	350
1.371	19300	32	1.047	61.8	17.0	440
1.647	23800	33	1.021	72.1	14.2	530
1.924	28300	33	1.002	82.2	12.2	610
2.197	32800	33	0.988	92.3	10.7	700

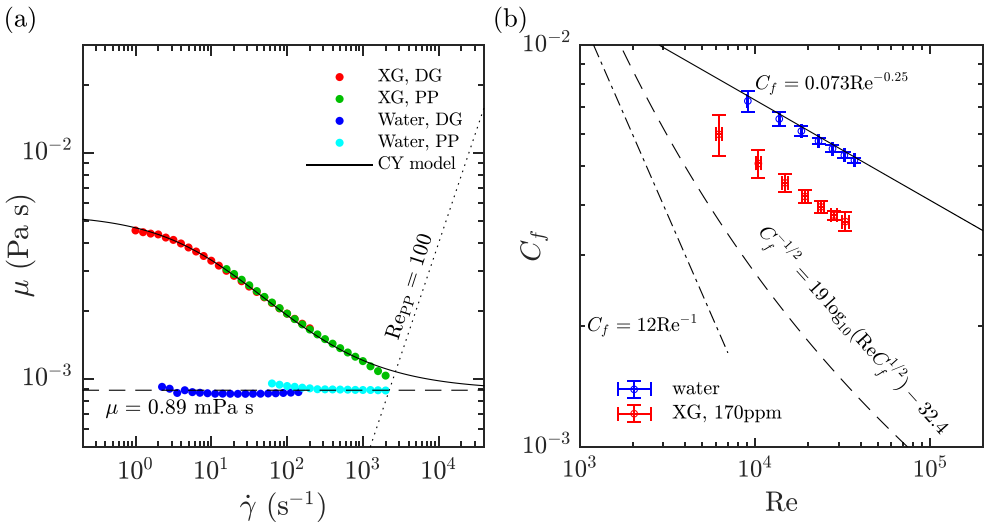

FIG. 2. (a) Steady shear viscosity measurements of 170 ppm XG solution and water. (b) Skin-friction coefficient as a function of Reynolds number for water and the 170 ppm XG solution.

C. Steady shear viscosity

Shear viscosity μ versus shear rate $\dot{\gamma}$ was measured for water and the 170 ppm XG solution using a torsional rheometer (HR-2, TA Instruments). Two geometries were used, a double-gap (DG) concentric cylinder for low to moderate $\dot{\gamma}$ and a parallel plate (PP) geometry for moderate to high $\dot{\gamma}$. The double-gap concentric cylinder consisted of four radii: an inner cup radius (15.1 mm), an inside bob radius (16.0 mm), an outside bob radius (17.5 mm), and an outside cup radius (18.5 mm). The sample was immersed in the cup and bob at a height of 53.0 mm. The PP geometry had a radius R of 30 mm. The gap height between the plates h_{PP} was set to 200 μm.

Figure 2(a) displays measurements of μ as a function of $\dot{\gamma}$ for the 170 ppm XG solution and water at 25 °C. The μ for water was measured between $\dot{\gamma}$ of 2 and 140 s^{-1} using the DG geometry and $\dot{\gamma}$ between 60 and 2000 s^{-1} using the PP geometry. For the rigid polymer solution, measurements of μ using the DG geometry are presented for 0.8 s^{-1} $< \dot{\gamma} <$ 180 s^{-1}. Results using the PP geometry were performed between $\dot{\gamma}$ of 10 and 2500 s^{-1} for the XG solution. The lower limit of $\dot{\gamma}$ for the viscosity measurements is a result of the low-torque limit of the rheometer [39]. The upper limit is a result of secondary or inertial flow instabilities that produce an increase in the measured torque and hence tamper with the measurements of μ. In the DG geometry, the secondary instabilities are Taylor vortices, while for the PP geometry secondary instabilities are radial flows or turbulence [39]. Davies and Stokes [40] demonstrated that secondary flows tampered with the PP measurements when the Reynolds number $\mathrm{Re}_{PP} = \rho\Omega R h_{PP}/\mu$ was greater than 100. Here Ω is the angular velocity of the upper plate in radians per second. Therefore, measurements of μ using the PP geometry with $\mathrm{Re}_{PP} > 100$ were disregarded. Measurements using the PP geometry at low h_{PP} can also be subjected to errors caused by gap offsets and surface tension [39–41]. Appendix A critically evaluates the consistency in measurements of μ for different gap heights and with alterations in the surface tension of the fluid by adding a small amount of Tween 20 to the XG solution. We observed that measurements of μ were consistent for different h_{PP}, the $\mathrm{Re}_{PP} = 100$ conservatively predicted the onset of inertial instabilities for different h_{PP}, and Tween 20 had little influence on the measurements of μ. Based on the results presented in Appendix A, we concluded that gap offset errors were minimal, the assumed inertial limitation from Davies and Stokes [40] was valid, and surface tension did not corrupt the measurements of μ.

The average and standard deviations in measurements of μ for water were 0.86 mPa s $\pm$ 3.2%. The average value of μ for water was approximately 3.5% different from the theoretical viscosity of water at 25 °C, i.e., 0.89 mPa s [37,38]. Therefore, a 3.5% relative systematic uncertainty was assumed for all measurements of μ, including measurements of the XG solution. This uncertainty propagates to other variables, including those used for inner normalization of flow velocity.

The trend in μ as a function of $\dot{\gamma}$ for the XG solution, shown in Fig. 2(a), was well approximated by the Carreau-Yasuda (CY) model

$$\frac{\mu - \mu_\infty}{\mu_0 - \mu_\infty} = \frac{1}{[1 + (\lambda_{\mathrm{CY}}\dot{\gamma})^a]^{n/a}}, \tag{1}$$

where μ_0 is the zero-shear-rate viscosity, μ_∞ is the infinite-shear-rate viscosity, λ_{CY} is a fitting constant with dimension of time, n is a dimensionless exponent, and a is a fitting parameter introduced by Yasuda *et al.* [25,26]. A Levenberg-Marquardt nonlinear least-squares method was used to fit Eq. (1) to the measurements of μ as a function of $\dot{\gamma}$ in MATLAB. The resulting CY fit for the XG solution had a μ_0 of 5.4 mPa s, μ_∞ of 0.89 mPa s, λ_{CY} of 0.11 s, n of 0.55 s, and a of 0.67. Equation (1) with these values is shown for reference in Fig. 2(a) by the black solid line. The root mean square (rms) in the absolute deviation between the measurements and the CY model was 0.05 mPa s. The rms of the relative deviation was 2.1%. This was considered a relative random uncertainty in the measurements of μ for XG. Together with the 3.5% systematic uncertainty assumed from our viscosity measurements of water, the total relative uncertainty in our measurements of μ for XG was conservatively assumed to be 5.6%.

D. Skin-friction coefficient and drag reduction

Plots of the skin-friction coefficient $C_f = 2\tau_w/\rho U_b^2$ as a function of Re are shown for water and XG in Fig. 2(b). To determine C_f for the XG flows, the wall shear stress had to first be established. The τ_w of each rigid polymer flow condition was derived based on measurements of ΔP. The near-wall shear rate $\dot{\gamma}_w$ was determined invoking the CY model coupled with pressure drop measurements by substituting $\mu_w = \tau_w/\dot{\gamma}_w$ into the left-hand side of Eq. (2) and using $\tau_w = h\Delta P/\Delta x$, after which the values of $\mu_w = \tau_w/\dot{\gamma}_w$ of each XG flow were determined. Subsequently, the variables Re, u_τ, λ, and Re_τ were obtained, all of which are listed in Table II for the rigid polymer flows. The resulting values of Re were then used in plots of C_f shown in Fig. 2(b). Error bars in the data points of C_f as a function of Re propagate from random errors in measurements of U_b and ΔP, as well as the assumed uncertainty in μ_w determined in the preceding section.

Measurements of C_f for water and XG show consistency with previous investigations. The equation $C_f = 0.073\,\mathrm{Re}^{-0.25}$, shown at the top of Fig. 2(b), is the empirical correlation relating C_f and Re for two-dimensional (2D) Newtonian turbulent channel flows prescribed by Dean [42]. The current measurements of C_f for water agree well with the equation derived by Dean [42] and are within 5% of the C_f power-law equation. The lower equation shown in Fig. 2(b) is the Virk MDR asymptote $C_f = 19\log_{10}(\mathrm{Re}C_f^{1/2}) - 32.4$ [43]. The measurements of C_f for the XG flows are between the C_f correlations of Dean [42] and Virk *et al.* [43]. Therefore, the XG flows do exhibit DR; however, none of the drag-reduced flows are at MDR. The C_f measurements for XG also reasonably agree with the expected trend for flows of type B drag-reducing additives with increasing Re. Virk and Wagger [11] detailed that type B additives exhibit a ladder effect, where the trend in C_f as a function of Re would be lower but parallel to the Newtonian C_f correlation equation. In Fig. 2(b) a trend in C_f for XG that is approximately parallel to the Dean [42] correlation with increasing Re can be observed.

Drag-reduction was quantified by the attenuation in τ_w of the polymer solution relative to a turbulent Newtonian flow of similar Re. The level of attenuation in τ_w was described by the percent

drag reduction

$$\mathcal{D} = 100\left(1 - \frac{\tau_{w,R}}{\tau_{w,N}}\right), \tag{2}$$

where $\tau_{w,R}$ is the wall shear stress of the rigid polymer solution and $\tau_{w,N}$ is the wall shear stress of a Newtonian fluid of similar Re. Comparing Newtonian and non-Newtonian fluids of like Re accounted for changes in the viscosity due to shear thinning [8,17,22]. Measurements of water and XG were performed at the same U_b and not Re. The Re are dissimilar considering XG has a higher shear viscosity than water, as demonstrated in Fig. 2(a). To establish a Newtonian value of $\tau_{w,N}$ that shares a common Re with the XG flows, $\tau_{w,N}$ was calculated using the equation of Dean [42] for C_f. The $\mathcal{D}$ was then subsequently determined for each flow condition of XG, the values for which are listed in Table II. As previously mentioned, the experimental measurements of C_f for water was within 5% of the Dean [42] skin-friction correlation. Therefore, using this equation to interpolate or extrapolate the C_f measurements of water was considered an adequate approximation.

The present investigation considers the reduction in $\Delta P/\Delta x$, at a fixed Re. Comparing different DR techniques is best done when a constant power input is maintained, where power is taken to be the product between Q and ΔP. Roccon *et al.* [44] considered a drag-reduced lubricated wall flow with a constant power input based on the procedure laid out by Hasegawa *et al.* [45]. Experimentally considering DR based on a constant power input is feasible, provided real-time measurements of the pressure gradient and volumetric flow rate are fed into a controller to maintain a constant power through manipulation of the flow rate. Such a procedure is not performed in the present investigation, but may yield better avenues for comparison between DNS and experiments with like conditions and across different DR techniques in the future. In addition, it is more relatable to industrial applications, which strive to mitigate energy dissipation, but also deliver more volumetric flow.

E. Planar particle image velocimetry

Planar PIV was used to characterize the velocity of the Newtonian and non-Newtonian channel flows. Images were collected using a digital camera (Imager Intense, LaVision GmbH) with a 1376×1040 pixel^2 charged-coupled device sensor. Each pixel was 6.45×6.45 μm^2 in size with a digital resolution of 12 bits. A reduced sensor size of 1376×605 pixel^2 was used to enable a higher image acquisition rate and therefore a faster convergence in velocity statistics. A Sigma lens with a focal length f of 105 mm and an aperture size of $f/8$ was used to focus on the full height of the channel at its midspan. The resulting magnification was 0.55, the depth of field was 1.30 mm, and the scaling factor was 11.81 μm pixel^{-1}. Figure 3 illustrates the flow measurement setup relative to the test section. The camera was arranged in a portrait orientation such that the 1376 pixel dimension of the sensor was parallel to the height of the channel. Therefore, the field of view (FOV) of the images was $(\Delta x, \Delta y) = 12.28\times16.25$ mm^2. Along the x direction, the center of the FOV was placed at the center of the glass test section, which is $107H$ downstream of the channel inlet.

The illumination source for the planar PIV measurements was a 90 mJ pulse^{-1} Nd:YAG laser (Gemini PIV 30, New Wave Research Inc.). Two spherical lenses (one concave, the other convex) and one concave cylindrical lens expanded the 4.5-mm diam beam output from the laser head into a 20-mm-wide (along the x direction) by 1-mm-thick (along the z direction) laser sheet at the measurement location. Silver-coated hollow glass spheres, 2 μm in diameter, were used to seed the flows (SG02S40 Potters Industries). Das and Ghaemi [46] demonstrated that these small silver-coated particles have strong side scattering and relatively consistent sizing. Synchronization between the camera and the laser was achieved using a programmable timing unit (PTU 9, LaVision GmbH) and DAVIS 7.3 software (LaVision GmbH). One data set consisted of 9000 pairs of double-frame images, recorded at an acquisition rate of 7.4 Hz. The time delay Δt between image frames was 50–400 μs depending on the Re of the flow. The specific value of Δt was chosen such that the maximum particle displacement between image frames was approximately 12 pixels.

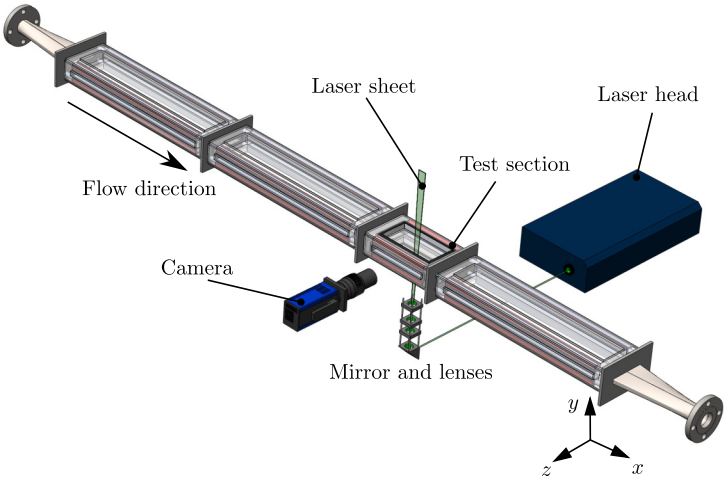

FIG. 3. Isometric three-dimensional model of the planar PIV setup relative to the glass test section and channel section.

All PIV processing was performed using DAVIS 8.4 software (LaVision GmbH). First, the minimum intensity of all images was subtracted from each image. Next, each data set was normalized with their respective average ensemble intensity. The instantaneous velocity vector was defined as $\boldsymbol{U}$. Its components along the streamwise and wall-normal directions were defined as U and V, respectively. Angular brackets were used to denote the ensemble average of the variables over time and the x direction. The latter averaging is applied due to the homogeneity of the fully developed turbulent channel flows in the streamwise direction. Fluctuations in the streamwise and wall-normal velocities were denoted by u and v, respectively. High spatial resolution profiles of mean streamwise velocity $\langle U \rangle$ were established using the ensemble-of-correlation method with a final interrogation window (IW) size of 6×6 pixel^2 (0.07×0.07 mm^2) and 83% overlap between neighboring IWs [47]. The resulting profiles of $\langle U \rangle$ had a single pixel spatial resolution (0.3λ–1.5λ, depending on Re). The lower limit of the measurements in $\langle U \rangle$ was $y = 35$ μm, which corresponds to $y^+ = 0.76$–3.15, depending on Re. The instantaneous velocities U and V were determined using a multipass cross-correlation algorithm with an initial IW size of 64×64 pixel^2 and a final IW size of 32×32 pixel^2 (0.38×0.38 mm^2), both with 75% overlap between adjacent IWs. The spatial resolution of instantaneous velocity measurements was 8 pixels or 0.09 mm (2λ–12λ). Vector postprocessing using the universal outlier detection algorithm developed by Westerweel and Scarano [48] was used to remove any spurious vectors in the measurements of U and V, after which the Reynolds normal stresses $\langle u^2 \rangle$ and $\langle v^2 \rangle$ and the Reynolds shear stress $\langle uv \rangle$ were determined. All first- and second-order velocity statistics attained reasonable statistical convergence with minimal random errors, as demonstrated in Appendix B.

The wall location was determined based on the local intensity maximum $I_{\max}$ that forms due to the glare line of the wall in the average intensity distribution of the PIV images. The uncertainty in the wall location was considered to be the extent of the high-intensity glare, which was assumed to be the Δy separating $I_{\max}$ and $I_{\max}/e^2$ [49]. The corresponding uncertainty in the wall location was estimated to be approximately 3 pixels or 35.4 μm (0.8λ–4.4λ). Errors in the wall location were treated as an uncertainty in y and were a contributing factor to the error bars in wall-normal distributions of mean velocity and Reynolds stresses.

Variables scaled using inner normalization were identified with the superscript $+$. Velocity statistics were normalized with the friction velocity $u_\tau = (\tau_w/\rho)^{1/2}$, positional coordinates were normalized with the wall units $\lambda = \mu_w/u_\tau\rho$, and viscosity variables were normalized by the wall viscosity μ_w, as listed in Tables I and II. Error propagation was used to derive the uncertainties in u_τ

and λ based on the assumed errors in μ_w (see Sec. II B) and random errors in ΔP. A conservative 0.1 pixel uncertainty in the PIV measurements of U and V was also assumed [50]. Such uncertainties in the inner scaling variables and the velocity measurements were reflected by error bars in plots of $\langle U\rangle^+$, $\langle u^2\rangle^+$, $\langle v^2\rangle^+$, and $\langle uv\rangle^+$.

F. Flow field analysis

Assuming the present XG solution follows the shear-thinning trend shown in Fig. 2(a), we obtained an approximation for the 2D instantaneous distribution of μ within the turbulent channel flow using the following procedure. First, a 2D version of the strain rate $\dot{\boldsymbol{\gamma}} = (2\boldsymbol{S} : \boldsymbol{S})^{1/2}$ was determined. Here $\boldsymbol{S} = (\boldsymbol{\nabla U} + \boldsymbol{\nabla U}^{\dagger})/2$ is the rate of strain tensor, the dagger denotes a matrix transpose, and the colon operator represents the double dot product of the rank-2 tensors. Considering the PIV vectors were two dimensional, $\dot{\boldsymbol{\gamma}}$ was determined using U and V alone, i.e., $\dot{\boldsymbol{\gamma}} = \{2[(\partial U/\partial x)^2 + 1/2(\partial U/\partial y + \partial V/\partial x)^2 + (\partial V/\partial y)^2]\}^{1/2}$. Therefore, our version of $\dot{\boldsymbol{\gamma}}$ was an approximation that does not take into account spanwise velocity W or spatial gradients along the spanwise direction. A moving second-order polynomial plane with a size of 40×40 pixel^2, or 0.45×0.45 mm^2, was fit along instantaneous distributions of U and V. Each 2D polynomial function was differentiated to obtain the spatial gradients in the velocity, i.e., $\partial U/\partial x$, $\partial U/\partial y$, $\partial V/\partial x$, and $\partial V/\partial y$. The 2D instantaneous distribution of μ was then established by substituting $\dot{\boldsymbol{\gamma}}$ into the CY model (1) that relates shear viscosity to shear rate for the XG solution. Time averaging was performed on the instantaneous viscosity profile to obtain a mean viscosity $\langle\mu\rangle$ and fluctuating viscosity $\mu' = \mu - \langle\mu\rangle$ similar to those derived in DNS using GN constitutive models [33–36], after which plots of the inner-normalized mean viscosity $\langle\mu\rangle^+ = \langle\mu\rangle/\mu_w$ and the inner-normalized root mean square of the fluctuating viscosity $\mathcal{R}(\mu')^+ = \sqrt{\langle\mu'^2\rangle}/\mu_w$ were determined. A two-point correlation of μ' was used to characterize the length scale of the viscosity fluctuations. The correlations coefficient $\rho_{\mu'\mu'}$ can be represented by the equation

$$\rho_{\mu'\mu'} = \frac{\langle\mu'(x_0, y_0)\,\mu'(x_0 + \delta x, y_0 + \delta y)\rangle}{\sqrt{\mu'^2(x_0, y_0)}\,\sqrt{\mu'^2(x_0 + \delta x, y_0 + \delta y)}}, \tag{3}$$

where (x_0, y_0) is the streamwise and wall-normal coordinate of the reference point and δx and δy represent the spatial shifts in the x and y directions, respectively. We considered two reference points, the first being $(x_0, y_0) = (0.1h, 0.07h)$ and the second being $(x_0, y_0) = (0.1h, 0.42h)$.

Assuming the GN constitutive model holds for XG and the 2D approximation of $\dot{\boldsymbol{\gamma}}$ is appropriate, the inner-normalized mean stress τ^+ across the half channel can be determined based on

$$\tau^+ = \tau_v^+ + \tau_v'^+ - \langle uv\rangle^+, \tag{4}$$

where $\tau_v^+ = \langle\mu\rangle^+\partial\langle U\rangle^+/\partial y^+$ is the mean viscous stress and $\tau_v'^+ = 2\langle\mu'^+ s_{xy}^+\rangle$ is the turbulent viscous stress, named by Singh *et al.* [33]. Note that $\boldsymbol{s} = \boldsymbol{S} - \langle\boldsymbol{S}\rangle$ is the fluctuating component of the rate of deformation tensor and $s_{xy} = (\partial u/\partial y + \partial v/\partial x)/2$. When normalized, $s_{xy}^+ = s_{xy}\lambda/u_\tau = s_{xy}/\dot{\gamma}_w$. Alternatively, the mean shear stress can be equally represented as $\tau^+ = 1 - y^+/\mathrm{Re}_\tau$. Previous investigations have referred to $\tau_v'^+$ as a polymer stress, estimated from the deficit $\tau_v'^+ = \tau^+ - \tau_v^+ + \langle uv\rangle^+$ [19,51]. Given that all components listed in Eq. (4) can be explicitly determined, the CY shear-thinning GN constitutive equation can be used to establish $\tau_v'^+$ and comment on its contribution to τ^+.

Another component of our analysis involved a spatial gradient in the mean velocity profile along y, i.e., $d\langle U\rangle/dy$. To remove high-frequency experimental noise and to differentiate the profile, a moving second-order polynomial filter was applied to the distribution of $\langle U\rangle$ with respect to y. The length of the filter was 24 pixels or 283 μm (6λ–35λ, depending on Re). Coefficients of the fitted second-order polynomial were used to calculate $d\langle U\rangle/dy$ and then established the indicator function $\zeta = y^+ d\langle U\rangle/dy^+$. Calculating $\langle\mu\rangle$ near the wall was limited by the spatial resolution of measurements in U and V. Better spatial resolutions were achieved in $\langle U\rangle$ due to the utilization of the ensemble-of-correlation method. To approximate $\langle\mu\rangle$ near the wall we assumed that the

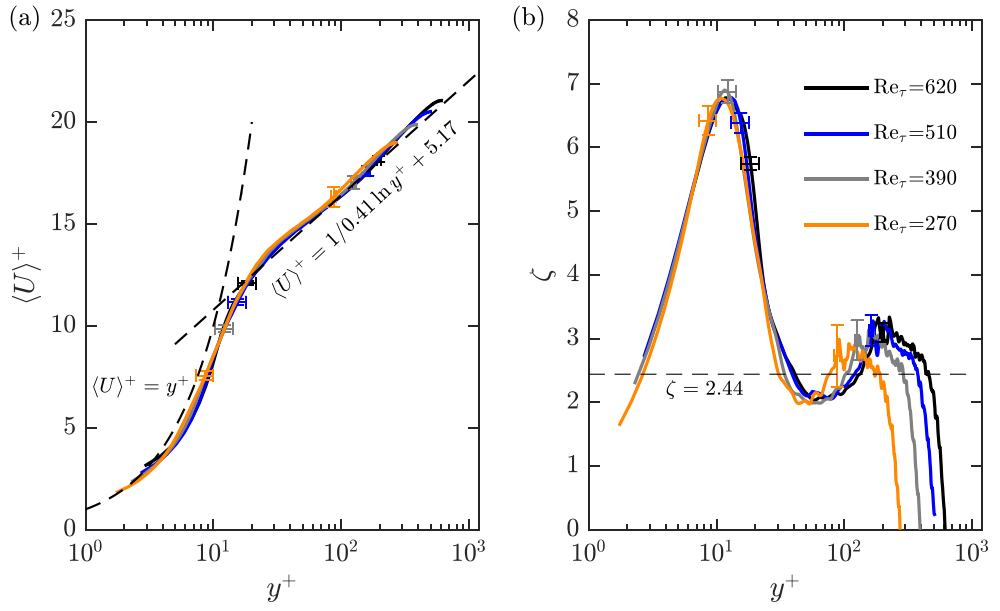

FIG. 4. Inner-normalized distributions of (a) mean streamwise velocity and (b) the indicator function, for Newtonian flows.

dominant component of $\dot{\boldsymbol{\gamma}}$ very close to the wall was $d\langle U\rangle/dy$. The wall-normal gradient in the mean viscosity was then substituted into the CY model to obtain an approximation of $\langle\mu\rangle$ near the wall. This is an assumption, one that is rather bold for a turbulent flow. As such, we refer to the profile as a pseudomean viscosity and denote it by $\tilde{\mu}$.

III. RESULTS

A. Newtonian turbulent channel flow

This section begins by comparing measurements of the mean velocity profiles for water with the Newtonian law of the wall in Fig. 4. For brevity, only experimental data for water with a Re_τ less than or equal to 620 are plotted. These conditions of Re_τ were chosen because they are similar in magnitude to the Re_τ conditions of the XG flows listed in Table II. Following the plots of $\langle U\rangle^+$, measurements of the Reynolds stresses for water are shown in Fig. 5. Three experimental Reynolds stress profiles with Re_τ of 270, 390, and 510 are presented on the same axes as the Reynolds stresses derived from Newtonian channel flow DNS by Iwamoto *et al.* [52] at $\mathrm{Re}_\tau = 300$ and Lee and Moser [53] at $\mathrm{Re}_\tau = 550$. The error bars in Figs. 4 and 5 are a result of uncertainties propagating from μ, ΔP, U, and y. For clarity, only two error bars are shown for each profile, one approximately in the buffer layer and the other within the outer layer.

Figure 4(a) demonstrates that all experimental profiles of water show good agreement with the law of the wall. The profiles were limited to $y > 35$ μm, which corresponds to $y^+ = 1.29$–2.89 for Re_τ between 270 and 620. For $y^+ < 5$ and greater than their respective lower limit, experimental measurements overlap with the profile of the linear viscous sublayer, $\langle U\rangle^+ = y^+$. Farther from the wall, all of the experimental distributions in Fig. 4(a) overlap with the logarithmic law $\langle U\rangle^+ = 1/\kappa \ln y^+ + B$. A von Kármán constant κ of 0.41 and intercept B of 5.17, as prescribed by Dean [42] for 2D Newtonian channel flows, is shown for comparison. Distributions of ζ shown in Fig. 4(b) accentuate the logarithmic dependence of $\langle U\rangle^+$ with respect to y^+. The profiles of ζ imply that κ is larger than 0.41 in the logarithmic layer for all profiles of water. Comparing the experimental profiles of $\langle U\rangle^+$ for different Re_τ, all distributions appear to overlap with one another within the

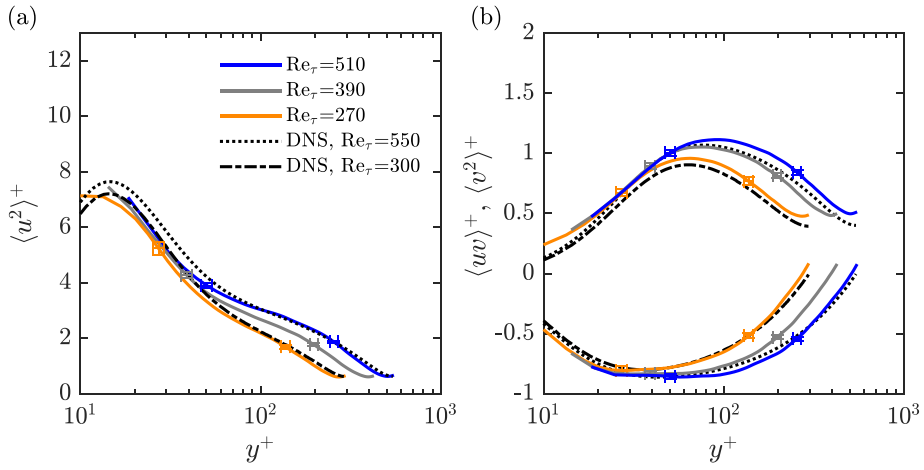

FIG. 5. Inner-normalized profiles of (a) streamwise Reynolds stress and (b) wall-normal and Reynolds shear stresses, for Newtonian flows.

boundaries of measurement uncertainties. The DNS of a Newtonian channel flow by Lee and Moser [53] demonstrated that profiles of $\langle U\rangle^+$ over a wider Re_τ range of 180–5000 also overlapped. The current experimental results for water also reflect universality in their distributions of $\langle U\rangle^+$ and ζ among different Re_τ.

Figure 5(a) presents experimental profiles of $\langle u^2\rangle^+$ relative to Newtonian channel flow DNS. For water with a $\mathrm{Re}_\tau = 510$, instantaneous PIV measurements with IWs of 32×32 pixel^2 and 75% overlap, which translates to a spatial resolution of 7.8λ. As a result, the linear viscous sublayer and a portion of the buffer layer is missed in these measurements. However, for lower Re_τ the spatial resolution of the measurements improve. The scenario with $\mathrm{Re}_\tau = 270$ has a spatial resolution of 3.5λ and has measurements that extend to wall-normal locations as small as $y^+ = 9$. Within the logarithmic and outer layers, the experimental results overlap with their DNS counterparts at similar Re_τ. The moderate $\mathrm{Re}_\tau = 390$ case demonstrates consistency, considering it lies between the two DNS and experimental profiles at lower and higher Re_τ. Figure 5(b) shows experimental and DNS profiles of $\langle v^2\rangle^+$ and $\langle uv\rangle^+$. Similar to the distributions in $\langle u^2\rangle^+$, experimental profiles in $\langle v^2\rangle^+$ and $\langle uv\rangle^+$ agree well with the DNS results at similar Re_τ. However, there are some small discrepancies. For example, the experimental profile of $\langle v^2\rangle^+$ at $\mathrm{Re}_\tau = 510$ appears to be minutely larger than the DNS profile of $\langle v^2\rangle^+$ at $\mathrm{Re}_\tau = 550$ for $y^+ > 100$. Overall, the experimental mean velocity and Reynolds stress measurements show consistency and agreement with 2D Newtonian channel flow DNS. Therefore, we can proceed to the results of the non-Newtonian solution with relatively good confidence in the validity of the measurements. It should also be noted that the spatial resolution of the measurements will improve with the addition of polymers, considering $\mathcal{D}$ is coupled with a reduction in u_τ and an increase in λ. This can be observed by comparing the larger values of λ for XG flows with the λ values of water in Tables I and II.

B. Non-Newtonian turbulent channel flow

The current section investigates the turbulent flow of the XG solution with varying Re_τ. The section is divided into three portions. Section III B 1 presents a wall-normal distribution of the mean velocity profile $\langle U\rangle^+$, indicator function ζ, and pseudoviscosity profile $\tilde{\mu}$ obtained from the vector fields with high spatial resolution. Section III B 2 investigates spatial distributions of the viscosity derived from the 2D shear rate. Section III B 3 delves into the Reynolds stresses and viscous stresses of non-Newtonian flows at different Re_τ.

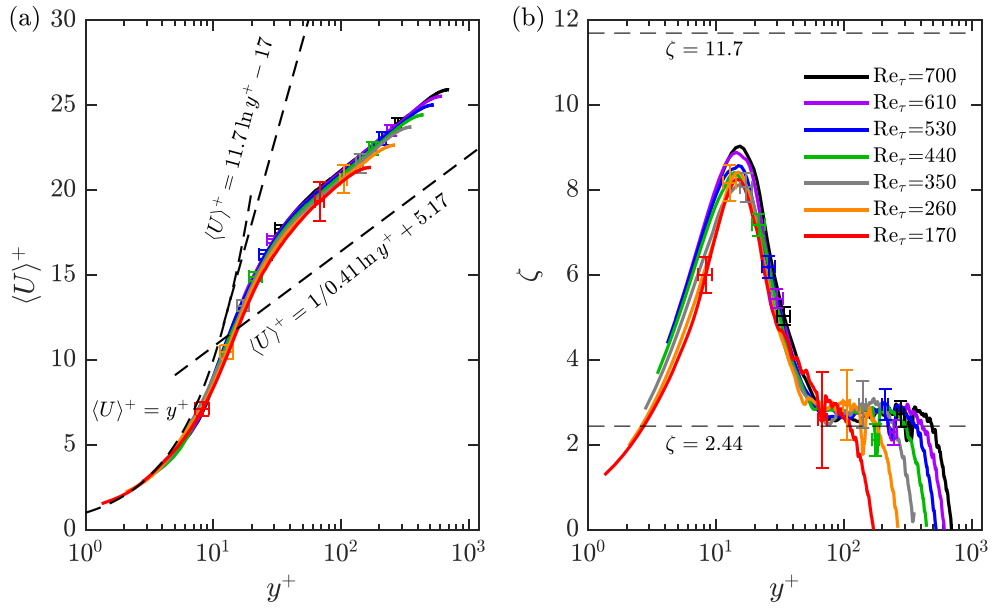

FIG. 6. Inner-normalized distributions of (a) mean streamwise velocity and (b) the indicator function, for flows with 170 ppm XG solution.

1. Mean velocity profile

Profiles of $\langle U\rangle^+$ for the XG scenarios are shown in Fig. 6(a). Near the wall, experimental distributions of $\langle U\rangle^+$ conform well with the linear viscous sublayer profile $y^+ = \langle U\rangle^+$ for all Re_τ under consideration. The upper limit of the linear viscous sublayer appears to grow relative to Newtonian wall turbulence. For a Newtonian turbulent channel flow, the linear approximation of the viscous sublayer is valid to within 10% at $y^+ = 5$ [54]. If a 10% confidence interval from $y^+ = \langle U\rangle^+$ is used as a threshold, we can approximate the size of the linear viscous sublayer for the non-Newtonian profiles shown in Fig. 6(a). Table III lists the size of the linear viscous sublayer for the flows, in both inner and outer scaling. The size in inner scaling is denoted by y_v^+, while the size in outer normalization is y_v/h. All values of y_v^+ are between 8 and 12, demonstrating that the linear viscous sublayer is expanded relative to Newtonian wall turbulence, which has a y_v^+ between 3 and 5 [54]. With increasing Re_τ, the non-Newtonian values of y_v^+ increase subtly, implying that the very-near-wall profiles might be slightly different and potentially depend on the small increase in $\mathcal{D}$ with increasing Re_τ, as shown in Table II. However, with error bars, these

TABLE III. Linear viscous sublayer sizes for non-Newtonian flows in inner and outer scaling.

Re_τ	y_v^+	y_v/h
170	8.3	0.051
260	9.1	0.036
350	10.1	0.030
440	10.8	0.025
530	11.5	0.023
610	11.2	0.019
700	11.4	0.017

differences could be a result of uncertainty in the measurements. At the larger Re_τ, between 530 and 700, the linear sublayer appears to saturate and nearly approach the trisection point $(y^+, \langle U\rangle^+) = (11.6, 11.6)$, where the Virk MDR asymptote $\langle U\rangle^+ = 11.7 \ln y^+ - 17$ intersects with $y^+ = \langle U\rangle^+$ and the Newtonian logarithmic law. Values of the outer-scaled thicknesses y_v/h decrease with increasing Re_τ, mainly due to the large shrinkage in y_v caused by increasing Re_τ.

Farther from the wall at $y^+ > 30$, Fig. 6(a) demonstrates a larger $\langle U\rangle^+$ relative to the logarithmic law of the wall, an observation common for drag-reduced flows. Virk [27] and later Warholic *et al.* [51] demonstrated that LDR flows form a Newtonian plug profile, which is observed as an increase in the logarithmic law intercept B but a similar κ, relative to the logarithmic law distribution of a Newtonian fluid. Virk [27] detailed that the growth in B was proportional with $\mathcal{D}$. A larger $\mathcal{D}$ would result in an increased buffer layer thickness (deemed the elastic sublayer) and hence an enhancement in B. Findings from Warholic *et al.* [51] showed that a Newtonian plug exists only for LDR flows with $\mathcal{D} < 35\%$. Given $\mathcal{D}$ of the present XG flows are between 27% and 33% (see Table II), the current XG flows satisfy the criteria for LDR. Therefore, our measurements agree well with previous observations of $\langle U\rangle^+$ profiles for polymer drag-reduced LDR flows. Furthermore, Fig. 6(a) demonstrates that profiles of $\langle U\rangle^+$ for XG have little dependence on Re_τ. There is perhaps a subtle increase in B for $170 < \mathrm{Re}_\tau < 440$; however, this could be attributed to the small growth in $\mathcal{D}$ with increasing Re_τ. The uncertainty in the flow measurements, shown by the error bars, also captures the small variations in B.

White *et al.* [55] reevaluated the efficacy of the Virk [27] elastic sublayer model using the indicator function ζ, which highlights regions of strong logarithmic dependence. They compared mean velocity profiles from various experimental and numerical investigations of different $\mathcal{D}$, canonical flows, and Re. For LDR flows, White *et al.* [55] observed constant ζ (generally for $y^+ > 50$), which is indicative of a Newtonian plug. Profiles of ζ shown in Fig. 6(b) also demonstrate regions of constant ζ, providing further evidence of a Newtonian plug for rigid polymer solutions. For all Re_τ, these regions of constant ζ are observed for $y^+ > 60$. This lower limit of $y^+ = 60$ is larger than the lower limit of $y^+ = 30$ for the Newtonian logarithmic layer [54], demonstrating an expansion of the viscous sublayer. The peak values of ζ for XG at $y^+ = 15$ are greater than the peak values of ζ for water as shown in Fig. 4(b). The implication is that the slope of $\langle U\rangle^+$ within the buffer layer is larger for flows of XG relative to water. A larger slope in $\langle U\rangle^+$ is indicative of an effective slip in the buffer layer, which in turn results in an increase in $\langle U\rangle^+$ within the logarithmic layer [27,56]. Another observation is that the constant value of ζ for the XG flows in the Newtonian plug layer are marginally larger than the values of ζ observed for water in the logarithmic layer shown in Fig. 4(b). White *et al.* [55] similarly observed that κ was slightly larger than water in the Newtonian plug for LDR flows. White *et al.* [55,57] broadly suggested that the inner-normalized mean velocity profile of a polymer drag-reduced flow depends on the Reynolds number, polymeric properties, and the canonical flow. We demonstrate that if $\mathcal{D}$ is constant, distributions of the inner-normalized mean velocity profiles of a rigid polymer solution are relatively independent of Re_τ within the inner layer of the flow.

Figure 7 demonstrates distributions of the normalized pseudoviscosity $\tilde{\mu}^+$ with respect to y^+ for the XG flows of different Re_τ. The profiles of $\tilde{\mu}$ are an approximation of the mean viscosity in the near-wall region. Intuitively, the decreasing trend in $\tilde{\mu}^+$ with increasing Re_τ at a given y^+ is plausible. Flows of higher Re_τ have larger $d\langle U\rangle/dy$; hence $\tilde{\mu}$ should be correspondingly lower relative to a flow of smaller Re_τ. For $y^+ < 10$, all XG flows have distributions of $\tilde{\mu}^+$ that are approximately constant, only growing subtly by about 1% with increasing y^+. As y^+ increases beyond 10 all profiles experience a dramatic increase in the magnitude of $\tilde{\mu}^+$. The precise y^+ location where this inflection in $\tilde{\mu}/\mu_w$ occurs depends on the Re_τ being considered. The thickness of the near-wall region of approximately constant $\tilde{\mu}$ appears to conform well with the peak in profiles of ζ, shown in Fig. 6(b) and indicative of the central location of the buffer layer. The inner-normalized thickness of this region of constant $\tilde{\mu}$ grows with increasing Re_τ. However, the value of $\tilde{\mu}^+$ appears to monotonically decrease with increasing Re_τ at any chosen value of y^+. Flows of large Re_τ experience a less aggressive change in $\tilde{\mu}$ with respect to y^+, but the size of

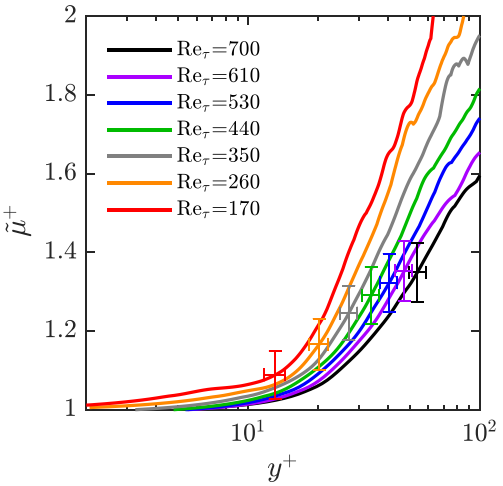

FIG. 7. Pseudomean viscosity normalized by wall viscosity as a function of inner-normalized wall location.

their near-wall region of low viscosity is larger. Generally, all flows experience a large and sudden change in $\tilde{\mu}$ for y^+ between 10 and 30. For example, the XG flow with $\mathrm{Re}_\tau = 170$ has a $\tilde{\mu}$ that is 50% larger than μ_w at $y^+ = 30$. A near-wall region of constant mean viscosity that suddenly and dramatically increases with respect to y^+ has also been observed from numerical simulations using GN models [33–36]. Our results appear to qualitatively agree with the results of DNS using inelastic shear-thinning GN models near the wall [33–35]. This is despite the approximation used to derive the pseudoviscosity profile $\tilde{\mu}$ based on 2D velocity data.

2. Turbulent shear viscosity

Figure 8(a) shows an instantaneous contour of u for XG with Re_τ of 170, while Fig. 8(b) shows a snapshot of μ. The contours in Figs. 8(a) and 8(b) are extracted at the same time instance. In Fig. 8(a), zones of low- and high-speed flow are observed. Figure 8(b) demonstrates that the

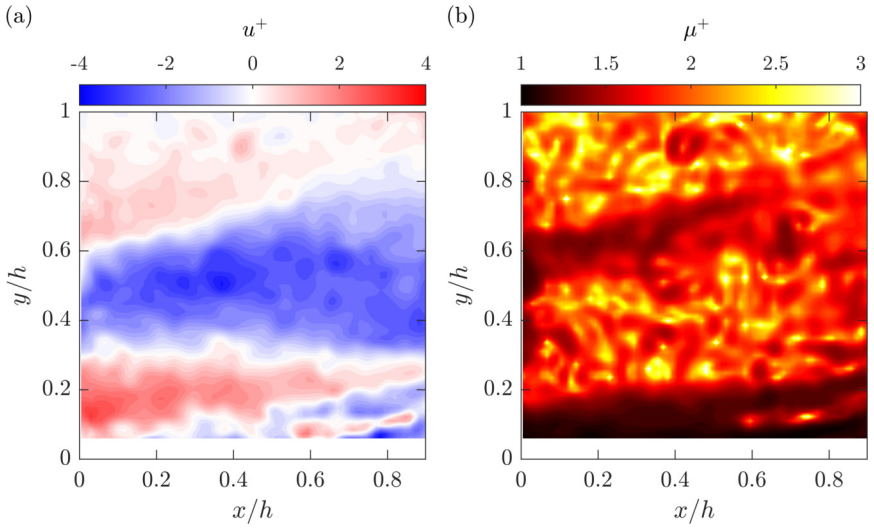

FIG. 8. Instantaneous contour of (a) streamwise velocity fluctuations and (b) viscosity for XG at $\mathrm{Re}_\tau = 170$.

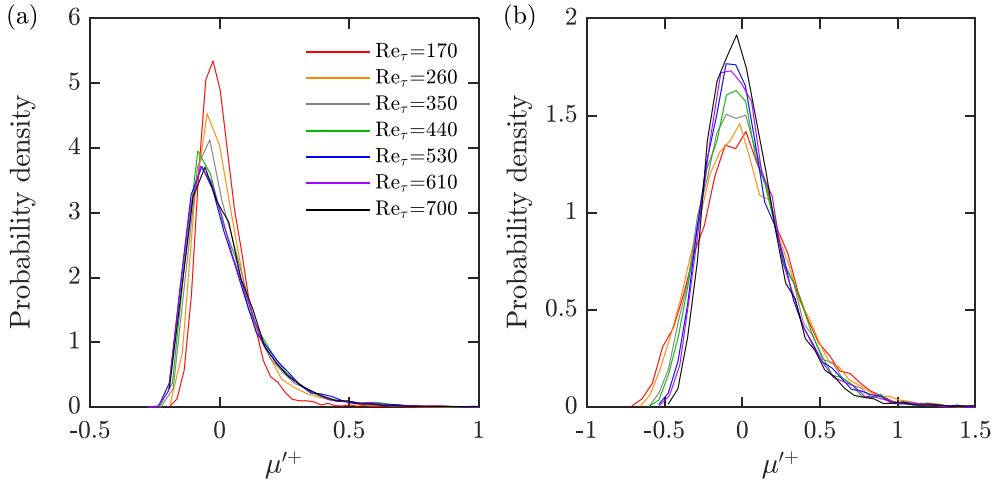

FIG. 9. Probability density function of fluctuating viscosity taken at x of $0.1h$ and y of (a) $0.07h$ and (b) $0.42h$.

viscosity near the wall is low and within 20% of μ_w for $y/h < 0.2$. Away from the wall, $y/h > 0.2$, most of the fluid has a μ between 1.5 and 3 times larger than μ_w. In general, the spatial distribution of μ shows large streamwise-elongated zones of low and high viscosity that contain small-scale viscosity fluctuations. For example a large, low-viscosity slug can be found at around $y/h = 0.6$ and extending from $x/h = 0$ to 0.6 in the snapshot shown in Fig. 8(b). The location of this low-viscosity slug appears to coincide roughly with the interface between the low- and high-speed zones, shown in Fig. 8(a). A second streamwise-elongated zone of low viscosity is observed extending from the wall at a shallow angle. Similarly, this low-viscosity zone overlaps with the shear layer between low- and high-speed zones.

Probability density functions (PDFs) of μ'^+ are shown in Fig. 9 for the XG flows at different Re_τ within the inner and outer layers of the flow. Figure 9(a) shows the PDFs of μ' at y/h of 0.07, while Fig. 9(b) shows the PDFs at y/h of 0.42. Within both the inner and outer layers of the flow, PDFs of μ'^+ are positively skewed. Within the inner layer, flows with smaller Re_τ (e.g., $\mathrm{Re}_\tau = 170$) tend to have a more narrow PDF than flows of larger Re_τ and demonstrate a smaller PDF peak. In contrast, Fig. 9(b) demonstrates that at $y/h = 0.42$, the peak PDF in μ'^+ is larger for flows of high Re_τ. This implies that viscosity fluctuations are likely larger for low-Re_τ flows within the outer layer. Wall-normal profiles of $\langle\mu\rangle^+$ and $\mathcal{R}(\mu')^+$ better demonstrate these differences.

Figure 10 provides inner-normalized profiles of the mean viscosity $\langle\mu\rangle^+$ and the rms of μ' for the non-Newtonian flows of different Re_τ. Figure 10(a) shows that distributions of $\langle\mu\rangle^+$ appear to be logarithmic, consistent with DNS using GN constitutive models [33–36]. The profiles of $\langle\mu\rangle^+$ for different Re_τ do not overlap; flows with lower Re_τ have larger $\langle\mu\rangle^+$ in the outer layer of the flow. Figure 10(b) shows the inner-normalized rms profiles of μ', which also reflect a dependence similar to that of $\langle\mu\rangle^+$ with respect to Re_τ. Unlike the present findings of Fig. 10, Singh *et al.* [34] observed that $\langle\mu\rangle^+$ and the $\mathcal{R}(\mu')^+$ overlapped for pipe flow DNS with a power-law GN model. We suspect the overlap is contingent on the choice of the rheological model, i.e., the power-law model. The nominal wall viscosities listed in Table II encroach on the second Newtonian regime of the CY model and are likely not well described by a power-law equation. Therefore, it appears that μ_w is an insufficient scaling parameter. Nonetheless, distributions of $\langle\mu\rangle^+$ demonstrate a lower average viscosity near the surface and a substantially higher viscosity closer to the core, much like the implication of the $\tilde{\mu}^+$ profiles shown in Fig. 7.

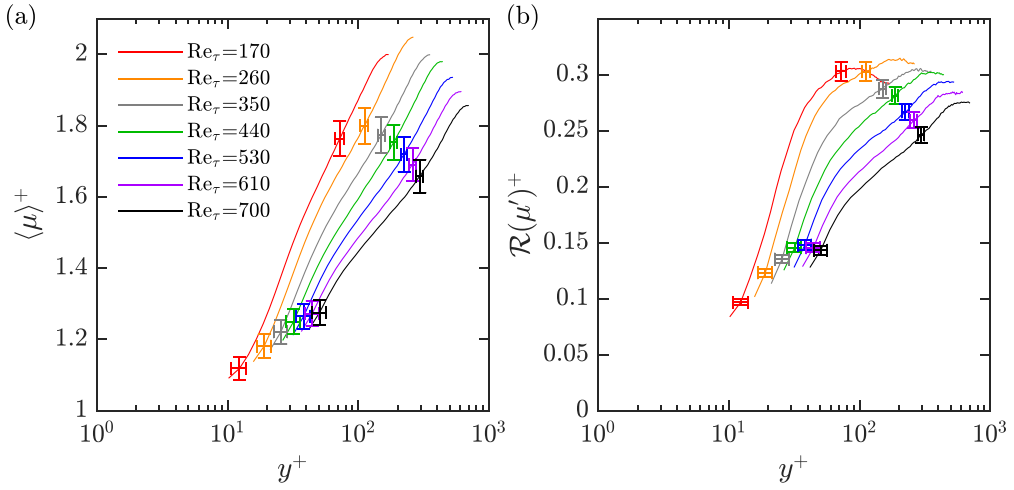

FIG. 10. Wall-normal profiles of (a) mean viscosity and (b) the root mean square of the fluctuating viscosity. Error bars are shown at y/h of 0.07 and 0.42.

To characterize the length scale of the viscous fluctuations, a two-point correlation of μ' using Eq. (3) was performed for each of the XG channel flows with different Re_τ. As mentioned in Sec. II F, two reference points were considered, the first being $(x_0, y_0) = (0.1h, 0.07h)$ and the second being $(x_0, y_0) = (0.1h, 0.42h)$. Therefore, the first point falls within the inner layer of the channel flow, while the second point is well into the outer layer of each flow ($y/h > 0.1$).

Figure 11(a) demonstrates distributions of the correlation coefficient $\rho_{\mu'\mu'}$ along the streamwise direction δx and at y/h of 0.07. Although Fig. 11 does not show the value of δx at which $\rho_{\mu'\mu'}$ becomes zero, it can be reasonably inferred that the size of the viscosity fluctuations along the x direction decrease in magnitude with increasing Re_τ. The same observation can be made in the outer layer based on plots of $\rho_{\mu'\mu'}$ as a function of δx and at a constant y/h of 0.42, shown in Fig. 11(b). Figure 12 presents profiles of $\rho_{\mu'\mu'}$ at x/h of 0.1 and along the wall-normal direction δy. For all Re_τ, $\rho_{\mu'\mu'}$ decays to zero within $0.06h$ when y_0 is $0.07h$, as shown in Fig. 12(a). For

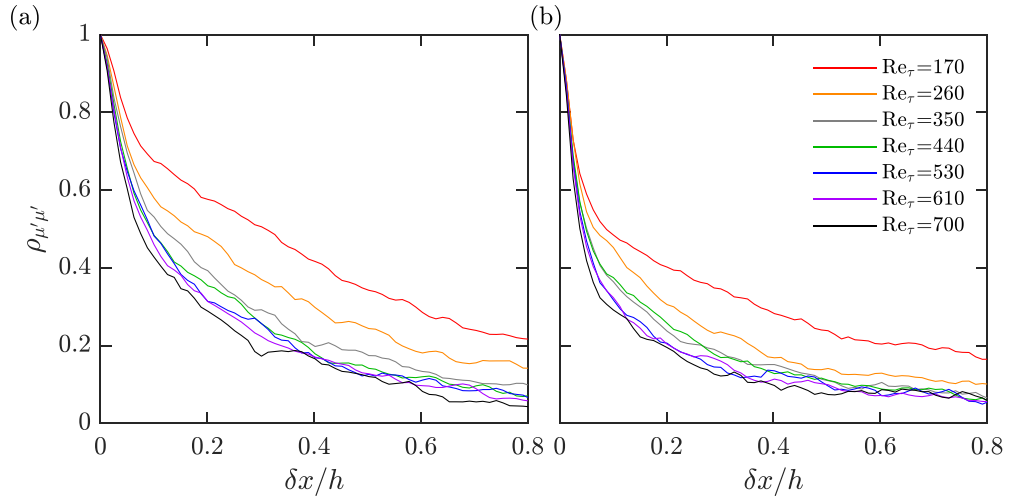

FIG. 11. Two-point correlation of viscosity fluctuations along the streamwise direction at wall-normal locations of (a) $y/h = 0.07$ and (b) $y/h = 0.42$.

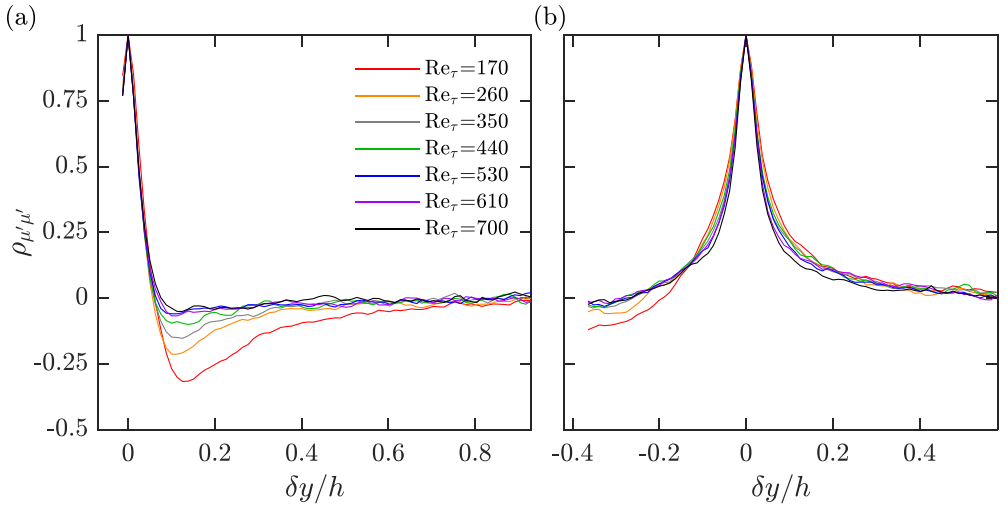

FIG. 12. Two-point correlation of viscosity fluctuations along the wall-normal direction with a reference wall-normal location of (a) $y_0 = 0.07h$ and (b) $y_0 = 0.42$.

lower Re_τ cases (e.g., 170 and 260), there is a significant anticorrelation between $\delta y/h$ of 0.06 and 0.2. The anticorrelation indicates a streaky pattern in the viscosity field, potentially generated by the shear layer structures between the streamwise-elongated low- and high-speed zones. We suspect this prevalent anticorrelation cannot be observed for large Re_τ due to the choice of y_0. For the case with the lowest Re_τ of 170, $y_0 = 0.07h$ is equivalent to a y^+ of 12, which lies near the center of the buffer layer or the peak in ζ. For $\mathrm{Re}_\tau = 700$, a y_0 of $0.07h$ corresponds to a y^+ of 49, which is close to the upper y^+ limit of the buffer layer. Therefore, μ' within the viscous sublayer appears to be opposite in sign convention to μ' within the logarithmic and outer regions of the flow. When y_0 is set to $0.42h$, profiles of $\rho_{\mu'\mu'}$ are generally the same for all Re_τ cases, shown in Fig. 12(b). The correlation coefficient attains a value of zero, or very close to zero (less than 0.01), within δy of $0.3h$. Based on Fig. 8(d), viscosity fluctuations are marginally more elongated along the x direction relative to y. The size of the structures become more isotropic with growing distance from the wall.

3. Reynolds stresses and mean shear stress budget

Figure 13(a) presents plots of $\langle u^2\rangle^+$ for the XG flows alongside experimental data of water with $\mathrm{Re}_\tau = 510$ and Newtonian channel flow DNS from Lee and Moser [53] with $\mathrm{Re}_\tau = 550$. Unlike the experimental results for water shown in Fig. 5(a), the peak in $\langle u^2\rangle^+$ could be resolved for at least the two lowest Re_τ scenarios, i.e., $\mathrm{Re}_\tau = 170$ and 260. The use of XG makes resolving the peak in $\langle u^2\rangle^+$ easier, since drag-reducing additives have been shown to shift the peak in $\langle u^2\rangle^+$ farther from the wall relative to Newtonian fluids [22,51]. In general, the magnitude in $\langle u^2\rangle^+$ for all Re_τ scenarios is increased relative to the experimental profile for water shown in Fig. 13(a). The amount by which the XG profile of $\langle u^2\rangle^+$ increases depends on the Re_τ being considered. For example, comparing XG and water at similar Re_τ of 510, the XG profile of $\langle u^2\rangle^+$ is larger for nearly all y^+.

Profiles of $\langle v^2\rangle^+$ are the positive distributions shown in Fig. 13(b). Relative to Newtonian profiles of similar Re_τ, distributions of $\langle v^2\rangle^+$ for the XG solutions demonstrate significant attenuation along all values of y^+. This can easily be seen by comparing the plots of $\langle v^2\rangle^+$ for XG at $\mathrm{Re}_\tau = 530$ with the experimental profile of water at $\mathrm{Re}_\tau = 510$. Distributions of $\langle uv\rangle^+$ correspond to the negative profiles shown in Fig. 13(b). Unlike $\langle v^2\rangle^+$, profiles of $\langle uv\rangle^+$ are only strongly attenuated near the wall, relative to Newtonian distributions of comparable Re_τ. The values of $\langle uv\rangle^+$ are similar for $y^+ > 150$ when comparing XG and water at a Re_τ of 510, while for $y^+ < 150$, the XG solution shows a large reduction in the magnitude of $\langle uv\rangle^+$ when contrasted with the profile of water with a

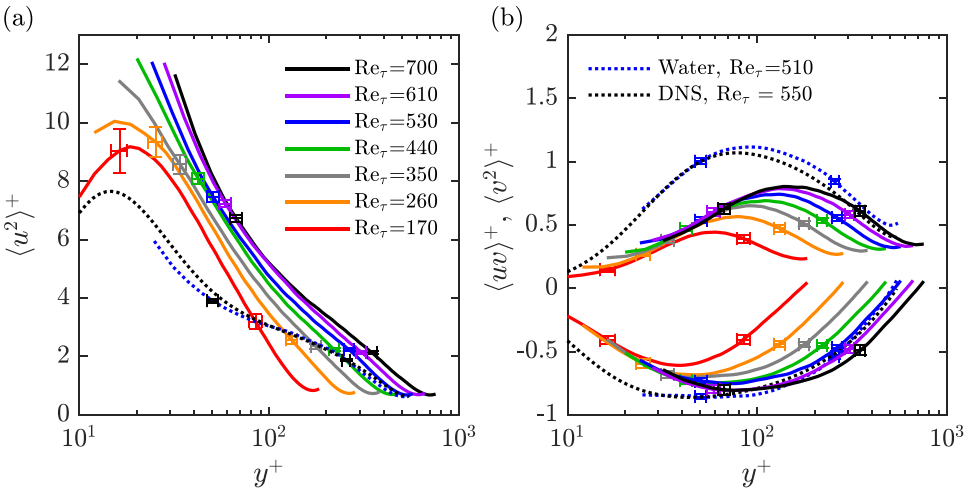

FIG. 13. Inner-normalized profiles of (a) streamwise Reynolds stress and (b) wall-normal and Reynolds shear stresses, for flows with 170 ppm XG solution.

similar Re_τ of 510. Therefore, relative to Newtonian profiles of similar Re_τ, solutions of XG at LDR exhibit strong attenuation in $\langle v^2\rangle^+$ throughout the complete half channel; however, attenuation in $\langle uv\rangle^+$ is confined to a portion of the channel near the wall. Comparing the Reynolds stress profiles of XG with one another, all distributions for XG shown in Fig. 13 increase in magnitude monotonically with increasing Re_τ at a given y^+, similar to the trend in the Reynolds stresses for Newtonian fluids of increasing Re_τ.

Different components of the mean stress balance are presented in Fig. 14. For brevity and to avoid clutter, the mean stress balance is shown for only three of the seven Re_τ cases (170, 440, and 700) of XG. The XG flows exhibit a trade-off in the budget or contribution of τ_v^+ and $-\langle uv\rangle^+$ to the total mean stress τ^+ depending on the y^+ location. Specifically, near the wall τ_v^+ contributes more to τ^+ than $-\langle uv\rangle^+$, while closer to the core of the channel, the opposite can be observed, i.e.,

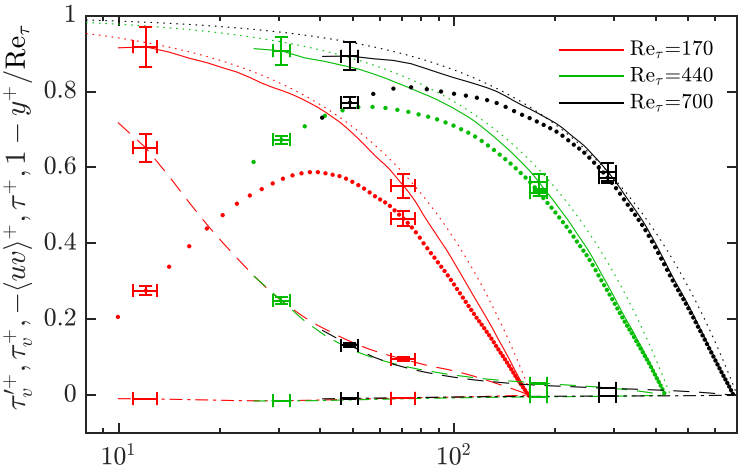

FIG. 14. Inner-normalized mean stress balance of XG at three of the seven Re_τ conditions. The lines correspond to $\cdots$, $1-y^+/\mathrm{Re}_\tau$;——, τ^+; ● ● ●, $\langle uv\rangle^+$;– –, τ_v^+; and – ·, $\tau_v'^+$. Error bars are shown at y/h of 0.07 and 0.42.

$-\langle uv\rangle^+$ is larger than τ_v^+. For all XG flows, the turbulent viscous stress $\tau_v'^+$ contributes little to τ^+, regardless of the y^+ location being considered. Distributions of τ^+, represented by the solid lines in Fig. 14 and determined from the summation of τ_v^+, $\tau_v'^+$, and $-\langle uv\rangle^+$ [i.e., Eq. (4)], agree well with $1 - y^+/\mathrm{Re}_\tau$ within the margin of experimental uncertainty, represented by the downsampled error bars. Therefore, we can assume measurements of τ_v^+, $\langle uv\rangle^+$, and $\tau_v'^+$ are approximately valid. Arosemena *et al.* [35,36] demonstrated that $\tau_v'^+$ accounted for less than 5% of τ^+ within the inner layer, based on DNS using a channel flow with a shear-thinning GN constitutive model that had $\mathcal{D} \approx 10\%$. Although the present non-Newtonian flows have almost three times the $\mathcal{D}$ as Arosemena *et al.* [35,36], $\tau_v'^+$ also appears to be less than 5% for XG. Therefore, a drag-reduced turbulent flow of XG can largely be explained by Reynolds and viscous stresses, with very little influence from stresses imposed by the fluctuating non-Newtonian viscosity.

In summary, the rigid polymer solution demonstrated larger profiles in $\langle U\rangle^+$ within the logarithmic layer relative to water, conducive of a Newtonian plug. Non-Newtonian flows of different Re_τ and similar $\mathcal{D}$ had overlapping profiles in $\langle U\rangle^+$, within the margin of measurement uncertainty. When compared to experiments of Newtonian turbulence at a similar Re_τ, XG exhibited larger profiles in $\langle u^2\rangle^+$ and smaller profiles in $\langle v^2\rangle^+$ for all y^+. Attenuation in $\langle uv\rangle^+$ was observable, but only near the wall. These findings are similar to those of numerical investigations using inelastic models, such as the GN power-law or Carreau constitutive equations. Singh *et al.* [34] used a power-law model to simulate an inelastic non-Newtonian turbulent pipe flow of Re_τ between 323 and 750. Constant material properties were maintained across their different cases of Re_τ to evaluate the effect of Re on the flow statistics, much like what is demonstrated in the present experimental investigation. Singh *et al.* [34] observed a Newtonian plug for all flow conditions, profiles of $\langle U\rangle^+$ that overlapped across different Re_τ, an enhancement in $\langle u^2\rangle^+$, attenuation in the radial and azimuthal Reynolds stresses, and a confined near-wall attenuation in $\langle uv\rangle^+$, relative to a Newtonian flow of similar Re_τ. Contrasting this with experiments using flexible polymers or DNS using elastic models, such as FENE-P, the same observations can be made for mean velocity statistics of generally any LDR flow, including the current findings. Consistency in the mean velocity statistics of elastic and inelastic DR suggests that the net effect of DR using elastic or inelastic additives is the same, at least for flows at LDR. This is despite their dramatically different rheology and potentially unique mechanisms for mitigating drag.

IV. DISCUSSION OF THE LUBRICATING LAYER

The classical theories of polymer DR have insinuated that polymers interact with turbulence in a manner that quells regions of high strain and vorticity through either an enhanced extensional viscosity or elasticity [14,15]. Indeed, experiments with flexible polymers in isotropic homogeneous grid turbulence demonstrate suppression of the small-scale turbulent eddies that correspond to regions of the flow with high extensional strain and thus high extensional viscosities [58]. However, shear-thinning properties of rigid polymers work against these postulates, in that regions with high shear rates have lower viscosities, not enhanced. A comparison of isotropic turbulence using FENE-P versus inelastic shear-thinning constitutive models could directly contrast the local instantaneous effect of flexible and rigid polymers on turbulence. Rather, we argue that the phenomenon of DR for inelastic shear-thinning fluids is primarily attributed to a wall-normal gradient in shear viscosity induced from the wall. Numerical investigations that employ inelastic shear-thinning constitutive models seem to support this claim. Arosemena *et al.* [36] performed channel flow DNS using an inelastic Carreau constitutive model and commented on the near-wall turbulent structures within the flow. They demonstrated that forces arising from fluctuations in the viscosity do not necessarily act in opposition of turbulent structures, such as quasistreamwise vortices and low- and high-speed streaks. Instead, Arosemena *et al.* [36] surmised that the local enhancement in the viscosity with increasing distance from the wall produces less energetic vortices and DR.

In the present experimental investigation, evidence of a striking demarcation in the viscosity, as well as the viscosity fluctuations, with growing distance from the wall are observed. For

example, Figs. 7, 8(b), and 10(a) imply that the viscosity within the outer layer of the channel can be 20%–300% higher than the nominal wall viscosity. Figures 11 and 12 demonstrate that the size of correlated viscosity fluctuations are thin ($\delta y/h \approx 0.06$) and long ($\delta x/h > 0.4$) within the buffer layer, but become more isotropic with increasing y. Moreover, spatial two-point correlations along the wall-normal direction show an anticorrelation between viscosity fluctuations within the near-wall region and the outer layer of the flow. It is apparent that the characteristics of the viscosity field are considerably different between the inner and outer layers of the flow. Furthermore, the mean stress balance, shown in Fig. 14, demonstrates that DR can largely be accounted for by a balance between viscous and Reynolds stresses alone, with little dependence on turbulent viscous stresses that arise from viscosity fluctuations. What is common among the present experimental investigation and DNS involving inelastic GN fluids [33–36] is a thin layer of nearly constant low-viscosity fluid close to the wall followed by a sharp increase in the mean viscosity with increasing distance from the wall.

This thin near-wall layer of low viscosity is perhaps analogous to the low-viscosity lubricating layer in the DNS of Roccon *et al.* [59]. In this numerical investigation, a thin layer of immiscible fluid with a different viscosity was introduced in the near-wall region. When the near-wall region had a viscosity comparable to that of the bulk fluid, Roccon *et al.* [59] observed that the surface tension between the two fluids produced DR. However, for the cases where the near-wall fluid had a lower viscosity, they commented that the near-wall fluid acts as a lubricating layer that results in a lower wall friction and consequently DR. In addition to this observation, there are some notable similarities with respect to the present investigation. In their DNS, Roccon *et al.* [59] demonstrated that the average thickness of the lubricating layer was similar to the thickness of the expanded linear viscous sublayer, y_v/h, in the present experimental findings for XG. The DNS by Roccon *et al.* [59] attained $\mathcal{D}$ of 24% with a lubricating layer that was $0.038h$ in thickness, a value comparable to those of y_v/h for XG, which are between $0.017h$ and $0.051h$, as listed in Table III. However, we should note that the $\mathcal{D}$ measured by Roccon *et al.* [59] is based on a enhancement of volumetric flow rate considering they maintain a constant pressure gradient in their DNS, similar to most numerical investigations involving turbulent DR, including those of Arosomena *et al.* [35,36] using GN constitutive models. In contrast, the present investigation considers a constant Re and evaluates the change in pressure gradient (a saving of "money" according to Frohnapfel *et al.* [60]).

Turbulent DR using shear-thinning liquids may also share commonalities with DR using superhydrophobic surfaces. Adding microscale roughness to a hydrophobic material produces a thin layer of air between the liquid and the solid boundary [61]. The air layer causes the moving liquid to "slip," generally resulting in large quantities of DR [62,63]. This apparent slip of the liquid phase produces a mean velocity profile where values of $\langle U\rangle^+$ are larger for all y^+, but parallel to the Newtonian law of the wall, seemingly reminiscent of the Newtonian plug in polymer DR. Indeed, Lumley [56] and Virk [27] regarded the Newtonian plug for polymer DR as being an effective slip. The Newtonian plug is realized in a polymer drag-reduced flow when the logarithmic layer is displaced upward to larger $\langle U\rangle^+$ [27]. The Newtonian plug and the effective slip were alluded to in the results pertaining to profiles of $\langle U\rangle^+$ and were realized by the large peak in ζ. For rigid polymer solutions, slippage and the Newtonian plug are perhaps manifestations of the fluid's shear-thinning rheology and the near-wall lubricating layer.

V. CONCLUSION

Solutions of xanthan gum polymer have historically demonstrated little viscoelastic and extensional properties, two rheological features often attributed to polymer drag reduction. Few existing experimental investigations have demonstrated the turbulence statistics of rigid polymers in a turbulent channel flow. The primary objective of our investigation was to scrutinize the effect of varying Reynolds number Re on the mean velocity and Reynolds stress profiles, independent of

change in DR. Our second objective was to evaluate the wall-normal gradient in the shear viscosity for drag-reduced flows of rigid polymers.

Measurements of the mean velocity profile and Reynolds stresses for an aqueous XG solution at friction Reynolds numbers Re_τ between 170 and 700 were provided. Compared to flows of similar Re, the XG solution exhibited drag-reduction percentages $\mathcal{D}$, between 27% and 33% with varying Re_τ. The XG solution reflected $\mathcal{D}$ with little dependence on the Re and skin-friction coefficient values, consistent with previous observations of DR using type B additives. A torsional rheometer equipped with a double-gap concentric cylinder and a parallel plate was used to measure the shear viscosity for shear rates between 1 and 2500 s^{-1}. A Carreau-Yasuda fit was used to model the shear viscosity curve.

Inner-normalized mean velocity profiles for the XG flows of different Re_τ approximately overlapped. This observation demonstrated that the inner-normalized mean velocity profiles are independent of Re_τ for a constant DR. Relative to the Newtonian law of the wall, the intercept of the logarithmic layer was considerably larger and the slope demonstrated marginal growth (i.e., a Newtonian plug flow). Compared to Newtonian Reynolds stress profiles of similar Re_τ, distributions for XG exhibited enhancement in streamwise Reynolds stresses and attenuation in wall-normal Reynolds stresses for all inner-normalized wall-normal coordinates. Attenuation in the Reynolds shear stress was only observed near the wall. The effect of increasing Re_τ in the non-Newtonian flows was the same as that in Newtonian flows, i.e., the Reynolds stresses increased in the logarithmic layer monotonically with increasing Re_τ. The modification to the first- and second-order velocity statistics reflected consistency with results obtained from DNS using elastic and inelastic constitutive models and previous experiments with flexible polymers.

The CY model and the spatial gradient in the velocity were used to approximate the instantaneous viscosity of each drag-reduced flow. All XG flows possessed a near-wall region that was thin and had a low mean viscosity. Fluid at wall-normal locations immediately above this region demonstrated dramatic growth in the mean viscosity. Viscosity fluctuations similarly reflected different size and characteristics with increasing distance from the wall. However, these viscosity fluctuations were shown to have a negligible contribution to the mean stress balance of the flow. Instead, DR was primarily driven by a trade-off between viscous and turbulent Reynolds stresses in the budget of mean stress. We referred to the thin low-viscosity layer as a lubricating layer, analogous to the wall-normal viscosity stratification observed in lubricated wall-bounded flows of immiscible fluids. This lubricating layer encapsulated the expanded linear viscous sublayer and portions of the buffer layer for flows of the XG solution. Its extent corresponded roughly to the peak in the indicator function ζ. Unlike the classical theories of polymer DR, we hypothesize that rigid polymer DR is largely attributed to gradients in the mean velocity coupled with the solution's shear-thinning rheology. The lubricating layer is a by-product of this interaction and a mechanism for generating an effective slip within the buffer layer.

ACKNOWLEDGMENT

The authors acknowledge support from the Natural Sciences and Engineering Research Council of Canada (Grant No. RGPIN-2020-07231).

APPENDIX A: INFLUENCE OF GAP HEIGHT AND SURFACE TENSION ON PARALLEL-PLATE SHEAR RHEOLOGY

Steady shear viscosity measurements using a parallel plate geometry can be subjected to several sources of error, especially when dealing with small gap heights h_{PP} [39,40]. Inertial flow instabilities, viscous heating, gap offsets, and surface tension are some of the many factors that can corrupt the viscosity measurements. Techniques have been introduced to correct or account for these errors. For example, gap offset errors can be corrected by measuring μ for different h_{PP} [40]. Measurements of μ at different h_{PP} are shown for the 170 ppm XG solution in Fig. 15. In this figure,

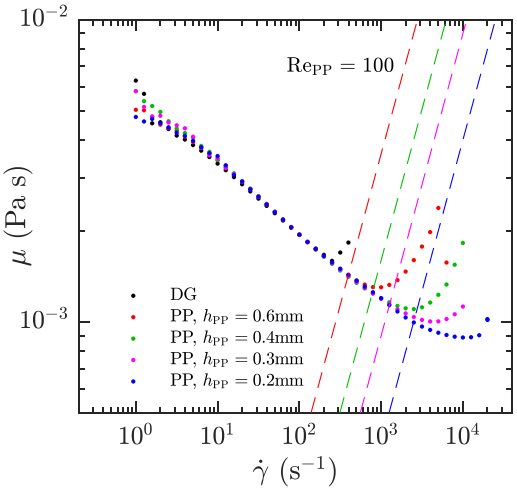

FIG. 15. Shear rheology of the 170 ppm XG solution measured for the PP geometry with different h_{PP}.

the upper shear rate threshold depended on the gap height and measurements were often terminated due to radial ejection of the fluid from the sides of the plates. Secondary flow instabilities are well demonstrated by the steep increase in μ at high $\dot{\gamma}$. The $\mathrm{Re_{PP}} = 100$ threshold [40], demonstrated by the color-coordinated dashed lines in Fig. 15, conservatively estimated the critical $\dot{\gamma}$ at which the inertial instabilities corrupted the measurements of μ. At $\dot{\gamma}$ between 10 and 2500 s^{-1} and ignoring viscosity measurement with $\mathrm{Re_{PP}} > 100$, the measurements of μ for different h_{PP} are in good agreement; therefore, gap offset errors were considered negligible when $\mathrm{Re_{PP}} < 100$.

Surface tension can corrupt measurements of μ using the PP geometry when rotational symmetry is not maintained. The most likely scenario where this may occur is when the fluid sample is improperly added between the plates (sample underfilling or overfilling) [41]. To identify if interfacial tension influenced the measurements of μ, we performed additional viscosity measurements that compared the 170 ppm XG solution with and without a small amount of Tween 20 (CAS 9005-64-5,

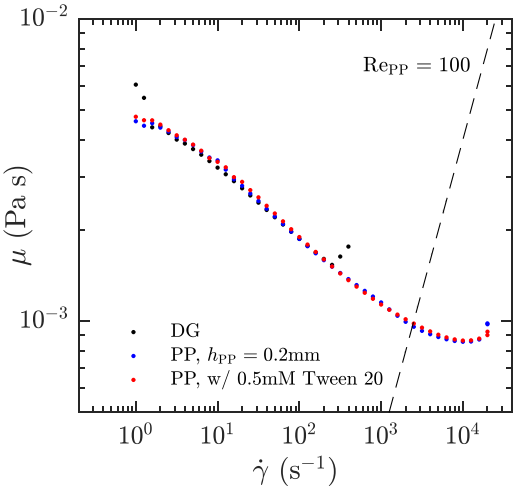

FIG. 16. Shear rheology of the 170 ppm XG solution measured for the PP geometry with and without Tween 20 and an h_{PP} of 0.2 mm.

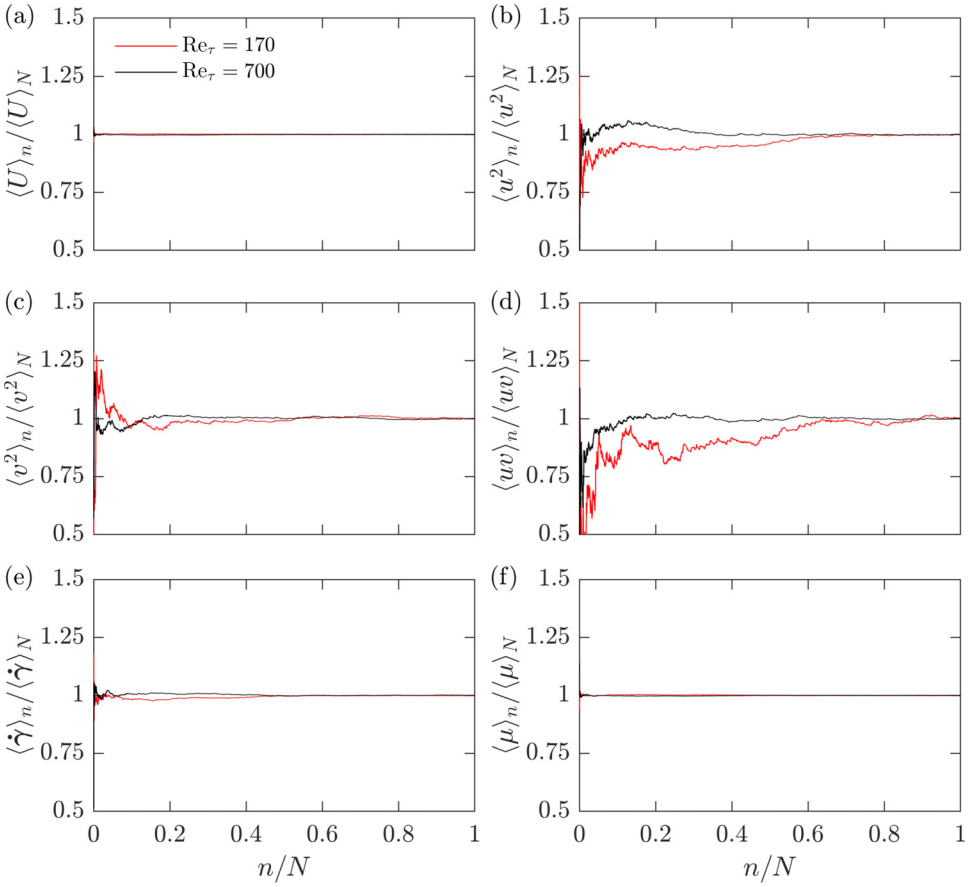

FIG. 17. Statistical convergence of (a) $\langle U\rangle$, (b) $\langle u^2\rangle$, (c) $\langle v^2\rangle$, (d) $\langle uv\rangle$, (e) $\langle\dot{\gamma}\rangle$, and (f) $\langle\mu\rangle$, for the flow of XG at its smallest and largest Re_τ cases of 170 and 700 and at a y^+ of 100.

Sigma Aldrich). Bąk and Podgórska [64] performed interfacial tension measurements of various aqueous Tween 20 solutions. They observed that a Tween 20 concentration of 0.2 mM reduced the interfacial tension of water by about 30% and a concentration of 0.6 mM reduced the surface tension of water by 40%. The XG solution was given enough Tween 20 to achieve a concentration of 0.5 mM. Based on the work of Bąk and Podgórska [64], a Tween 20 concentration of 0.5 mM would have a significant influence on the surface tension of the solution. Figure 16 demonstrates the measurements of the XG solution with and without Tween 20 at h_{PP} of 0.2 mm. There is good agreement among the measurements of μ using the DG geometry and the PP geometry with and without Tween 20. Therefore, we can confidently assume that the solution was loaded properly into the PP and surface tension has little influence on the shear viscosity measurements.

Although using the PP allowed us to obtain measurements of μ for much higher $\dot{\gamma}$ than we would have otherwise been able to achieve using just the DG geometry, there are more ideal measurement techniques for obtaining high-shear-rate viscometry. For example, microfluidic channels or dedicated high-shear-rate rheometers can obtain viscosity measurements for $\dot{\gamma}$ on the order of 10^5 s^{-1} with high accuracy and a low probability for human error. Pipe *et al.* [65] were able to measure μ for $\dot{\gamma}$ up to 80 000 s^{-1} using a microfabricated channel. Similarly, Sepulveda *et al.* [66] measured the viscosity of various XG solutions using a microfluidic rheometer for $\dot{\gamma}$ up to 2×10^5 s^{-1}. Utilizing such measurement techniques could yield better quality of the CY fit and more certainty in the near-wall scaling.

TABLE IV. Random error estimated from the range in the convergence of $n/N = 0.8$ to 1, for the velocity statistics of XG at its smallest and largest Re_τ cases of 170 and 700 and for y^+ of 50, 100, and 200.

Re_τ	y^+	$\langle U \rangle$	$\langle u^2 \rangle$	$\langle v^2 \rangle$	$\langle uv \rangle$	$\langle \dot{\boldsymbol{\gamma}} \rangle$	$\langle \mu \rangle$
170	50	0.13%	1.00%	0.69%	1.45%	0.37%	0.11%
170	100	0.05%	1.09%	1.24%	2.91%	0.49%	0.11%
170	200	0.03%	0.78%	0.65%	4.83%	0.21%	0.04%
700	50	0.07%	0.63%	1.47%	1.67%	0.25%	0.08%
700	100	0.08%	0.83%	0.55%	1.09%	0.22%	0.06%
700	200	0.03%	0.59%	0.62%	0.93%	0.37%	0.11%

APPENDIX B: STATISTICAL CONVERGENCE

Figure 17 demonstrates the convergence distributions of the first- and second-order statistics of velocity, as well as $\dot{\boldsymbol{\gamma}}$ and μ, for XG with Re_τ of 170 and 700 and at a y^+ location of 100. The variable n denotes an instantaneous data point, while N is the total number of data points. Variables with a subscript of n, i.e., $\langle \cdots \rangle_n$, represent the average from the first data point to the nth data point. Each convergence plot is normalized with their respective average over the complete ensemble of data points $\langle \cdots \rangle_N$. All distributions converge to the ensemble average approximately within the last 20% of the data (from $n/N = 0.8$ to 1). A random error is calculated by determining the range (maximum subtracted from the minimum) in the convergence from n/N of 0.8 to 1, the results of which are shown in Table IV. The random errors for y^+ of 50 and 200 are also provided. Generally all random errors listed in Table IV are less than 5%, implying good statistical convergence for all variables.

[1] B. Toms, in *Proceedings of the International Congress on Rheology* (North-Holland, Amsterdam, 1948), Vol. 2, pp. 135–141.

[2] J. M. J. den Toonder, A. A. Draad, G. D. C. Kuiken, and F. T. M. Nieuwstadt, Degradation effects of dilute polymer solutions on turbulent drag reduction in pipe flows, Appl. Sci. Res. **55**, 63 (1995).

[3] E. D. Burger, L. G. Chorn, and T. K. Perkins, Studies of drag reduction conducted over a broad range of pipeline conditions when flowing Prudhoe Bay crude oil, J. Rheol. **24**, 603 (1980).

[4] R. H. J. Sellin and M. Ollis, Polymer drag reduction in large pipes and sewers: Results of recent field trials, J. Rheol. **24**, 667 (1980).

[5] R. C. Figueredo and E. Sabadini, Firefighting foam stability: The effect of the drag reducer poly(ethylene) oxide, Colloids Surf. A **215**, 77 (2003).

[6] A. S. Pereira, R. M. Andrade, and E. J. Soares, Drag reduction induced by flexible and rigid molecules in a turbulent flow into a rotating cylindrical double gap device: Comparison between poly(ethylene oxide), polyacrylamide, and xanthan gum, J. Non-Newtonian Fluid Mech. **202**, 72 (2013).

[7] H.-W. Bewersdorff and R. P. Singh, Rheological and drag reduction characteristics of xanthan gum solutions, Rheol. Acta **27**, 617 (1988).

[8] A. Japper-Jaafar, M. P. Escudier, and R. J. Poole, Turbulent pipe flow of a drag-reducing rigid "rod-like" polymer solution, J. Non-Newtonian Fluid Mech. **161**, 86 (2009).

[9] E. J. Soares, R. N. Siqueira, L. M. Leal, K. C. Barbosa, D. F. Cipriano, and J. C. Freitas, The role played by the aging of aloe vera on its drag reduction properties in turbulent flows, J. Non-Newtonian Fluid Mech. **265**, 1 (2019).

[10] W. R. dos Santos, E. Spalenza Caser, E. J. Soares, and R. N. Siqueira, Drag reduction in turbulent flows by diutan gum: A very stable natural drag reducer, J. Non-Newtonian Fluid Mech. **276**, 104223 (2020).

[11] P. Virk and D. Wagger, in *Structure of Turbulence and Drag Reduction*, edited by A. Gyr (Springer, Berlin, 1990), pp. 201–213.

[12] M. Mohammadtabar, R. S. Sanders, and S. Ghaemi, Turbulent structures of non-Newtonian solutions containing rigid polymers, Phys. Fluids **29**, 103101 (2017).
[13] L. Warwaruk and S. Ghaemi, A direct comparison of turbulence in drag-reduced flows of polymers and surfactants, J. Fluid Mech. **917**, A7 (2021).
[14] J. L. Lumley, Drag reduction in turbulent flow by polymer additives, J. Polym. Sci. **7**, 263 (1973).
[15] P.-G. de Gennes, *Introduction to Polymer Dynamics* (Cambridge University Press, Cambridge, 1990).
[16] C. M. White and M. G. Mungal, Mechanics and prediction of turbulent drag reduction with polymer additives, Annu. Rev. Fluid Mech. **40**, 235 (2008).
[17] L. Xi, Turbulent drag reduction by polymer additives: Fundamentals and recent advances, Phys. Fluids **31**, 121302 (2019).
[18] B. E. Owolabi, D. J. C. Dennis, and R. J. Poole, Turbulent drag reduction by polymer additives in parallel-shear flows, J. Fluid Mech. **827**, R4 (2017).
[19] P. Ptasinski, B. Boersma, F. Nieuwstadt, M. Hulsen, H. Van den Brule, and J. Hunt, Turbulent channel flow near maximum drag reduction: Simulations, experiments and mechanisms, J. Fluid Mech. **490**, 251 (2003).
[20] T. Min, H. Choi, and J. Y. Yoo, Maximum drag reduction in a turbulent channel flow by polymer additives, J. Fluid Mech. **492**, 91 (2003).
[21] T. Min, J. Y. Yoo, H. Choi, and D. D. Joseph, Drag reduction by polymer additives in a turbulent channel flow, J. Fluid Mech. **486**, 213 (2003).
[22] M. Escudier, A. Nickson, and R. Poole, Turbulent flow of viscoelastic shear-thinning liquids through a rectangular duct: Quantification of turbulence anisotropy, J. Non-Newtonian Fluid Mech. **160**, 2 (2009).
[23] M. Mohammadtabar, R. Sanders, and S. Ghaemi, Viscoelastic properties of flexible and rigid polymers for turbulent drag reduction, J. Non-Newtonian Fluid Mech. **283**, 104347 (2020).
[24] H. Barnes, J. Hutton, and K. Walters, *An Introduction to Rheology* (Elsevier, Amsterdam, 1989).
[25] P. J. Carreau, Rheological equations from molecular network theories, Trans. Soc. Rheol. **16**, 99 (1972).
[26] K. Yasuda, R. C. Armstrong, and R. E. Cohen, Shear flow properties of concentrated solutions of linear and star branched polystyrenes, Rheol. Acta **20**, 163 (1981).
[27] P. S. Virk, An elastic sublayer model for drag reduction by dilute solutions of linear macromolecules, J. Fluid Mech. **45**, 417 (1971).
[28] L. Thais, T. B. Gatski, and G. Mompean, Some dynamical features of the turbulent flow of a viscoelastic fluid for reduced drag, J. Turbul. **13**, N19 (2012).
[29] V. S. L'vov, A. Pomyalov, I. Procaccia, and V. Tiberkevich, Drag Reduction by Polymers in Wall Bounded Turbulence, Phys. Rev. Lett. **92**, 244503 (2004).
[30] E. De Angelis, C. M. Casciola, V. S. L'vov, A. Pomyalov, I. Procaccia, and V. Tiberkevich, Drag reduction by a linear viscosity profile, Phys. Rev. E **70**, 055301(R) (2004).
[31] I. Procaccia, V. S. L'vov, and R. Benzi, Colloquium: Theory of drag reduction by polymers in wall-bounded turbulence, Rev. Mod. Phys. **80**, 225 (2008).
[32] M. Doi and S. Edwards, *The Theory of Polymer Dynamics* (Oxford University Press, New York, 1988).
[33] J. Singh, M. Rudman, and H. M. Blackburn, The influence of shear-dependent rheology on turbulent pipe flow, J. Fluid Mech. **822**, 848 (2017).
[34] J. Singh, M. Rudman, and H. M. Blackburn, Reynolds number effects in pipe flow turbulence of generalized Newtonian fluids, Phys. Rev. Fluids **3**, 094607 (2018).
[35] A. A. Arosemena, H. I. Andersson, and J. Solsvik, Turbulent channel flow of generalized Newtonian fluids at a low Reynolds number, J. Fluid Mech. **908**, A43 (2020).
[36] A. A. Arosemena, R. Andersson, H. I. Andersson, and J. Solsvik, Effects of shear-thinning rheology on near-wall turbulent structures, J. Fluid Mech. **925**, A37 (2021).
[37] A. Nagashima, Viscosity of water substance-new international formulation and its background, J. Phys. Chem. Ref. Data **6**, 1133 (1977).
[38] A. F. Collings and N. Bajenov, A high precision capillary viscometer and further relative results for the viscosity of water, Metrologia **19**, 61 (1983).
[39] R. H. Ewoldt, M. T. Johnston, and L. M. Caretta, *Experimental Challenges of Shear Rheology: How to Avoid Bad Data* (Springer, New York, 2015), pp. 207–241.

[40] G. Davies and J. Stokes, Thin film and high shear rheology of multiphase complex fluids, J. Non-Newtonian Fluid Mech. **148**, 73 (2008).
[41] M. T. Johnston and R. H. Ewoldt, Precision rheometry: Surface tension effects on low-torque measurements in rotational rheometers, J. Rheol. **57**, 1515 (2013).
[42] R. B. Dean, Reynolds number dependence of skin friction and other bulk flow variables in two-dimensional rectangular duct flow, J. Fluids Eng. **100**, 215 (1978).
[43] P. S. Virk, H. S. Mickley, and K. A. Smith, The ultimate asymptote and mean flow structure in Toms' phenomenon, J. Appl. Mech. **37**, 488 (1970).
[44] A. Roccon, F. Zonta, and Solda, Energy balance in lubricated drag-reduced turbulent channel flow, J. Fluid Mech. **911**, A37 (2021).
[45] Y. Hasegawa, M. Quadrio, and B. Frohnapfel, Numerical simulation of turbulent duct flows with constant power input, J. Fluid Mech. **750**, 191 (2014).
[46] P. Das and S. Ghaemi, Light-scattering of tracer particles for liquid flow measurements, Meas. Sci. Technol. **32**, 065302 (2021).
[47] C. J. Kähler, S. Scharnowski, and C. Cierpka, On the resolution limit of digital particle image velocimetry, Exp. Fluids **52**, 1629 (2012).
[48] J. Westerweel and F. Scarano, Universal outlier detection for PIV data, Exp. Fluids **39**, 1096 (2005).
[49] W. Abu Rowin, J. Hou, and S. Ghaemi, Inner and outer layer turbulence over a superhydrophobic surface with low roughness level at low Reynolds number, Phys. Fluids **29**, 095106 (2017).
[50] M. Raffel, C. E. Willert, F. Scarano, and C. J. Kähler, *Particle Image Velocimetry* (Springer, Berlin, 2018).
[51] M. D. Warholic, H. Massah, and T. J. Hanratty, Influence of drag-reducing polymers on turbulence: Effects of Reynolds number, concentration and mixing, Exp. Fluids **27**, 461 (1999).
[52] K. Iwamoto, Y. Suzuki, and N. Kasagi, Reynolds number effect on wall turbulence: Toward effective feedback control, Int. J. Heat Fluid Flow **23**, 678 (2002).
[53] M. Lee and R. D. Moser, Direct numerical simulation of turbulent channel flow up to $Re_\tau \approx 5200$, J. Fluid Mech. **774**, 395 (2015).
[54] S. Pope, *Turbulent Flows* (Cambridge University Press, Cambridge, 2000).
[55] C. M. White, Y. Dubief, and J. Klewicki, Re-examining the logarithmic dependence of the mean velocity distribution in polymer drag reduced wall-bounded flow, Phys. Fluids **24**, 021701 (2012).
[56] J. L. Lumley, Drag reduction by additives, Annu. Rev. Fluid Mech. **1**, 367 (1969).
[57] C. M. White, Y. Dubief, and J. Klewicki, Properties of the mean momentum balance in polymer drag-reduced channel flow, J. Fluid Mech. **834**, 409 (2018).
[58] E. van Doorn, C. M. White, and K. R. Sreenivasan, The decay of grid turbulence in polymer and surfactant solutions, Phys. Fluids **11**, 2387 (1999).
[59] A. Roccon, F. Zonta, and A. Soldati, Turbulent drag reduction by compliant lubricating layer, J. Fluid Mech. **863**, R1 (2019).
[60] B. Frohnapfel, Y. Hasegawa, and M. Quadrio, Money versus time: evaluation of flow control in terms of energy consumption and convenience, J. Fluid Mech. **700**, 406 (2012).
[61] J. P. Rothstein, Slip on superhydrophobic surfaces, Annu. Rev. Fluid Mech. **42**, 89 (2010).
[62] H. Ling, S. Srinivasan, K. Golovin, G. H. McKinley, A. Tuteja, and J. Katz, High-resolution velocity measurement in the inner part of turbulent boundary layers over super-hydrophobic surfaces, J. Fluid Mech. **801**, 670 (2016).
[63] W. Abu Rowin and S. Ghaemi, Streamwise and spanwise slip over a superhydrophobic surface, J. Fluid Mech. **870**, 1127 (2019).
[64] A. Bąk and W. Podgórska, Interfacial and surface tensions of toluene/water and air/water systems with nonionic surfactants Tween 20 and Tween 80, Colloids Surf. A **504**, 414 (2016).
[65] C. J. Pipe, T. S. Majmudar, and G. H. McKinley, High shear rate viscometry, Rheol. Acta **47**, 621 (2008).
[66] J. Sepulveda, A. Montillet, D. Della Valle, T. Amiar, H. Ranchon, C. Loisel, and A. Riaublanc, Experimental determination and modeling of flow curves of xanthan gum solutions over a large range of shear rates, Appl. Rheol. **31**, 24 (2021).